Improvement of Orographic Gravity Wave Parameterization Using a Mesoscale Gravity Wave Model

YOUNG-JOON KIM AND AKIO ARAKAWA

Department of Atmospheric Sciences, University of California, Los Angeles, California

(Manuscript received 1 September 1993, in final form 6 October 1994)

ABSTRACT

Parameterization of gravity waves due to subgrid-scale orography is now included in most existing large-scale models of the atmosphere. Parameterization schemes, however, have so far been evaluated mainly in view of the overall performance of the large-scale models. This may lead to an inappropriate assessment of the schemes since errors from various sources may interact with one another. To avoid this situation, an approach is taken in which a numerical model that explicitly resolves gravity waves is used to evaluate the performance of the schemes. For this purpose, a mesoscale two-dimensional nonlinear anelastic nonhydrostatic model is developed and used to numerically simulate gravity waves for a variety of orographic conditions. Regarding a subdomain of the mesoscale model as the horizontal grid interval of a large-scale model, two vertical profiles of gravity wave drag are compared—one for the subdomain-averaged values of the drag simulated by the mesoscale model and the other for the drag calculated by a parameterization scheme applied to the subdomain-averaged variables.

A test parameterization scheme is constructed by adopting the essential features of the existing schemes. An extensive evaluation of the test parameterization scheme with the aid of the dataset obtained from the mountain wave simulations shows that the scheme does not properly treat the enhancement of drag due to low-level wave breaking through the resonant amplification of nonhydrostatic waves. The authors show that the standard deviation of orography and the tuning coefficient in the scheme alone are not sufficient for properly representing this effect. The authors discuss the approach taken to overcome this deficiency by including additional statistical information on subgrid-scale orography in the input to the parameterization. A revised parameterization scheme constructed following this approach is presented.

1. Introduction

It has been recognized that parameterization of gravity waves due to subgrid-scale orography should be included in large-scale models of the atmosphere (e.g., Lilly 1972). It has been shown, for example, that excessively strong westerlies may appear in the midlatitude Northern Hemisphere in high-resolution winter simulations if gravity wave drag due to subgrid-scale orography is neglected. Currently, gravity wave parameterization schemes primarily based on the linear hydrostatic mountain wave theory together with the saturation hypothesis (Lindzen 1981) are widely used. [See Gates (1992) for a list of selected large-scale models that include gravity wave parameterization schemes.]

Table 1 compares orographic gravity wave parameterization schemes used mainly for the stratosphere and the troposphere. Boer et al. (1984) were the first to implement a gravity wave drag parameterization scheme in a large-scale model of the lower atmosphere. Chouinard et al. (1986) subsequently presented a scheme in which the (inverse) Froude number,[1] a measure of nonlinearity of orographic gravity waves, is used to determine the vertical distribution of drag. Palmer et al. (1986) and McFarlane (1987) independently developed schemes that utilize the saturation hypothesis to formulate the breaking of gravity waves. Schemes similar to those of Palmer et al. (e.g., Miller and Palmer 1986; Miller et al. 1989; Helfand et al. 1987; Iwasaki et al. 1989; Broccoli and Manabe 1992) and McFarlane (McFarlane et al. 1987) have been used in many other studies.

It is believed that the major mountain ranges simply act as barriers to the flow and do not significantly contribute to the mean surface drag. Considering this possibility of flow blocking as well as numerical stability, Palmer et al. (1986) posed an upper limit on the standard deviation (SD) of orography for the reference-level drag (see Table 1). Miller and Palmer (1986), McFarlane (1987), and McFarlane et al. (1987) used

---

Corresponding author address: Dr. Young-Joon Kim, Department of Atmospheric Sciences, University of California, 405 Hilgard Ave., Los Angeles, CA 90095.
E-mail: yjkim@yosemite.atmos.ucla.edu

[1] $Fr \equiv Nh/U$. (N is the Brunt–Väisälä frequency, h is the mountain height, and U is the horizontal wind.)

TABLE 1. Intercomparison of selected sub-grid-scale orographic gravity wave parameterization schemes used mainly for the stratosphere and the troposphere. Here, $Fr \equiv Nh/U$, $Ri \equiv N^2/(\delta U/\delta z)^2$.

Designer/user(s) (year) and institution(s)	Drag at the reference level (τ_0)	Residual drag above the reference level (τ)	Sub-grid-scale orographic gravity wave amplitude (h)	Tuning coefficient ($k = m/\Delta x$)	Criterion for Lindzen's wave saturation
Boer et al. (1984) Atmospheric Environment Service (AES)/Canadian Climate Center (CCC)	$-\bar{k}\rho_0 N_0 U_0 h$	$\tau_0 \dfrac{z_2 - z}{z_2 - z_1}$; $z_2 \geqslant z > z_1$, when convectively unstable.	$\dfrac{9 \times 10^8 C_f^2}{1 + 4 \times 10^5 C_f^2}$; $C_f = \mathrm{Max}(C_D - 1.5 \times 10^{-3}, 0)$ C_D = Cressman drag coef.	Effective aspect ratio of the orographic features.	Saturation hypothesis not used.
Chouinard et al. (1986) AES/CCC	$-\bar{k}\rho_0 N_0 U_0 h$	$\left(\dfrac{\partial U}{\partial t}\right)_{\mathrm{GWD}} \propto -U^2\,\mathrm{Max}\left\{1 - \dfrac{Fr_c^2}{Fr^2}, 0\right\}$	$2\sigma_h$ (σ_h; Standard deviation of sub-grid-scale orography.)	0.01	Saturation hypothesis not used, $Fr_c = \sqrt{0.5} = 0.71$
Palmer et al. (1986) United Kingdom Meteorological Office (UKMO)	$-k\rho_0 N_0 U_0 h^2$	$Fr_c^2 \dfrac{k\rho U^3}{N}$ if $Ri_m < Ri_c$; $Ri_m = Ri \dfrac{1 - Fr}{(1 + \sqrt{Ri}Fr)^2}$	$\mathrm{Min}(\sigma_h, 400\ \mathrm{m})$	$2.5 \times 10^{-5}\ \mathrm{m}^{-1}$	$Ri_c = 0.25$ [Fr_c (for $Ri \gg 1$) $= \sqrt{0.69} = 0.83$]
McFarlane (1987) AES/CCC	$-k\rho_0 N_0 U_0 h^2$	$\left(\dfrac{\partial U}{\partial t}\right)_{\mathrm{GWD}} \propto -\dfrac{U^3}{N}\mathrm{Max}\left[\dfrac{d\ \ln Fr^2(z)}{dz}, 0\right]$	$\mathrm{Min}\left(2\sigma_h, \mathrm{Fr}_c \dfrac{U_0}{N_0}\right)$	$8.0 \times 10^{-6}\ \mathrm{m}^{-1}$	$Fr_c = \sqrt{0.5} = 0.71$
Pierrehumbert (1986) Geophysical Fluid Dynamics Laboratory (GFDL)/National Oceanic and Atmospheric Administration (NOAA)	$-k \dfrac{\rho_0 U_0^3}{N_0} G(Fr)$; $G(Fr) \equiv \dfrac{Fr^2}{Fr^2 + 1}$ $\{Fr < Fr_c\}$ $\{\equiv 3 + 5(Fr - Fr_c)^2; Fr > Fr_c\}$	Decreasing linearly with height to zero.	σ_h	$\dfrac{1}{100\ \mathrm{km}}$ $= 1.0 \times 10^{-5}\ \mathrm{m}^{-1}$	Saturation hypothesis not used, $\{Fr_c = 0.8\}$
Miller and Palmer (1986), Miller et al. (1989) European Centre for Medium-Range Weather Forecasts (ECMWF) and UKMO	$-k\rho_0 N_0 U_0 h^2$	$-k\rho NUh_i^2$; $h_i = \left[\dfrac{\Delta x \tau_{i+1}}{m(\rho NU)_i}\right]^{1/2}$ $Ri_m = Ri \dfrac{1 - Fr}{(1 + \sqrt{Ri}Fr)^2}$	$[\mathrm{Min}(\lvert\sigma_h\rvert^2, \lvert\sigma_h^*\rvert^2)]^{1/2}$; $\lvert\sigma_h^*\rvert^2 = \lvert\sigma_h\rvert_{Ri_c}^2$ by MP, $\mathrm{Min}(\sigma_h, 400\ \mathrm{m})$ by MPS.	$2.5 \times 10^{-5}\ \mathrm{m}^{-1}$	$Ri_c = 0.25$
Stern et al. (1987) GFDL/NOAA	$-k \dfrac{\rho_0 U_0^3}{N_0} G(Fr)$; $G(Fr) = \dfrac{Fr^2}{Fr^2 + 1}$	$\tau_0\left[1 - \dfrac{p - p_0}{p_T - p_0}\right]$; $p_T > p > p_0$	σ_h	$\left[\mathrm{Min}\left(\Delta x, \dfrac{3U_0}{N_0}\right)\right]^{-1}$	Saturation hypothesis not used.
McFarlane et al. (1987) CCC and Canadian Meteorological Centre (CMC)	$-k\rho_0 N_0 U_0 h^2$	$-k\rho NUh_i^2$; $h_i = \left\{\mathrm{Min}\left[\dfrac{(\rho NUh^2)_{i+1}}{(\rho NU)_i}, \left(\dfrac{UFr_c}{N}\right)_i^2\right]\right\}^{1/2}$	$\mathrm{Min}\left(2\sigma_h, Fr_c \dfrac{U_0}{N_0}\right)$	$\dfrac{1}{125\ \mathrm{km}} = 8.0$ $\times 10^{-6}\ \mathrm{m}^{-1}$	$Fr_c = 0.7$

Helfand et al. (1987) National Aeronautic and Space Administration (NASA)/ Goddard Space Flight Center (GSFC)	$-k\rho_0 N_0 U_0 h^2$	$-k\rho NUh^2;\quad Fr_i^2 = \frac{\tau_{i+1}N_i}{k\rho_i U_i^3}$ $Ri_m = Ri(1 - Fr)$	$\mathrm{Min}\left(\mathrm{Min}(\sigma_h, 400\ \mathrm{m}), 0.85\frac{U_0}{N_0}\right)$	$2.5 \times 10^{-5}\ \mathrm{m}^{-1}$	$Ri_c = 0.25$ $\left[Fr_c = 1 - \frac{1}{4Ri}\right]$
Alpert et al. (1988) National Meteorological Center (NMC)/National Weather Service/NOAA	$-k\frac{\rho_0 U_0^3}{N_0}G(Fr);\ G(Fr) \equiv \frac{Fr^2}{Fr^2 + 1}$	$-k\rho NUh^2;\quad Fr_i^2 = \frac{\tau_{i+1}N_i}{k\rho_i U_i^3}$ $Ri_m = Ri(1 - Fr)$	σ_h	$\frac{1}{100\ \mathrm{km}}$ $= 1.0 \times 10^{-5}\ \mathrm{m}^{-1}$	$Ri_c = 0.25$ $\left[Fr_c = 1 - \frac{1}{4Ri}\right]$
Stern and Pierrehumbert (1988) GFDL	$-k\frac{\rho_0 U_0^3}{N_0}G(Fr);\ G(Fr) \equiv \frac{Fr^2}{Fr^2 + 1}$	$\tau_{\mathrm{sat}} = -k\rho U^2 DG;\quad D^{-2} = \frac{N^2}{U^2} - \frac{U_{zz}}{U}$ or $= \tau_0\left[1 - \frac{p - p_0}{p_T - p_0}\right]$	σ_h	$\frac{1}{100\ \mathrm{km}}$ $= 1.0 \times 10^{-5}\ \mathrm{m}^{-1}$	$\tau \geqslant \tau_{\mathrm{sat}}$ or no saturation hypothesis.
Iwasaki et al. (1989) Japanese Meteorological Agency	$-k\rho_0 N_0 U_0 h^2$	$-k_A\rho NUh^2$ $-k_B(\sigma - 0.3)^2;\quad \sigma \equiv \frac{p}{p_s} > 0.3$	$\mathrm{Min}\left(\sigma_h, 0.5Fr_c\frac{U_0}{N_0}\right)$	$2.0 \times 10^{-5}\ \mathrm{m}^{-1}$ for k_A $5.0 \times 10^{-5}\ \mathrm{m}^{-1}$ for k_B	$Fr_c = 1.0$
Surgi (1989) University of Miami	$-k\rho_0 N_m U_0 h^2;$ $N_m = \sqrt{1 - \epsilon}N_d\,(0 < \epsilon < 0.3)$	$-k\rho N_m Uh_i^2;\quad h_i = \left[\frac{\Delta x\tau_{i+1}}{m(\rho N_m U)_i}\right]^{1/2}$ $Ri_m = Ri\frac{1 - Fr}{(1 + \sqrt{Ri}Fr)^2}$	$\mathrm{Min}(\sigma_h, 400\ \mathrm{m})$	$2.5 \times 10^{-5}\ \mathrm{m}^{-1}$	$Ri_c = 0.25$
Hayashi et al. (1992) GFDL/NOAA	$-k\rho_0 N_0 U_0 h^2$	$\tau_0\frac{\sigma - \sigma_c}{1 - \sigma_c};\quad \sigma_c \leqslant \sigma \leqslant 1$	σ_h	$2.2 \times 10^{-5}\ \mathrm{m}^{-1}$	Saturation hypothesis not used.
A test scheme, constructed following Pierrehumbert (1986) and Miller and Palmer (1986)	$-\frac{m}{\Delta x}\frac{\rho_0 U_0^3}{N_0}G(Fr);$ $G(Fr) \equiv \frac{Fr^2}{Fr^2 + 1}$	$-k\rho NUh_i^2;\quad h_i = \left[\frac{\Delta x\tau_{i+1}}{m(\rho NU)_i}\right]^{1/2}$ $Ri_m = Ri\frac{1 - Fr}{(1 + \sqrt{Ri}Fr)^2}$	σ_h	$\frac{\Delta x}{L_m}$	$Ri_c = 0.25$
A revised scheme constructed in the present study	$-E\frac{m}{\Delta x}\frac{\rho_0 U_0^3}{N_0}\frac{Fr^2}{Fr^2 + C_G/\mathrm{OC}};$ $E \equiv (\mathrm{OA} + 2)^{C_E Fr_0/Fr_c}$	$-k\rho NUh_i^2;$ $h_i = \left[\frac{\Delta x\tau_{i+1}}{m(\rho NU)_i}\right]^{1/2}$ $Ri_m = Ri\frac{1 - Fr}{(1 + \sqrt{Ri}Fr)^2}$ $\frac{\tau_i}{\tau_{i+1}} = \mathrm{Min}\left[C_l\frac{l_i^2}{l_{i+1}^2}, 1\right];$ $\mathrm{OA} > 0, z < z_T.$	σ_h	$C_m\left[1 + \frac{\Sigma L_h}{\Delta x}\right]^{\mathrm{OA}+1};$ $C_m = 3.3 \times 10^{-5}\ \mathrm{m}^{-1},$ $C_E = 0.8,\quad C_G = 0.5,$ $C_l = 1,\quad z_T \approx 10\ \mathrm{km}$	$Ri_c = 0.25$ $Fr_c = 1.0$

more refined criteria for limiting SD, while Stern et al. (1987) limited the magnitude of a tuning coefficient in the parameterization scheme. Pierrehumbert (1986) proposed a flux function that gives a smooth transition between the blocking situation—for the flow with a large Froude number—and the nonblocking situation—for the flow with a small Froude number. Pierrehumbert's flux function has also been used in other studies (e.g., Stern et al. 1987; Stern and Pierrehumbert 1988; Alpert et al. 1988). For an easy comparison, the expressions for the treatment of the blocking effect are reproduced in Table 2.

TABLE 2. Treatment of blocking effects for the parameterization of orographic gravity wave drag. The term $\mathrm{SD}|^2 Ri_c$ is the solution of (4.6) with $Ri_m = Ri_c$, where the subscript c denotes the critical value. See Table 1 for complete schemes.

Method	Formula	Users
Limit on SD	Min(SD, 400 m)	Palmer et al. (1986) Miller et al. (1989) Helfand et al. (1987)
	$[\mathrm{Min}(\lvert\mathrm{SD}\rvert^2, \lvert\mathrm{SD}\rvert^2 Ri_c)]^{1/2}$	Miller and Palmer (1986)
	$\propto\mathrm{Min}(2\mathrm{SD}, Fr_c U/N)$	McFarlane (1987) McFarlane et al. (1987) Iwasaki et al. (1989)
Limit on k $(=m/\Delta x)$	$[\mathrm{Min}(\Delta x, 3U/N)]^{-1}$	Stern et al. (1987)
Asymptotic flux function	$G(Fr) \equiv \frac{Fr^2}{Fr^2 + 1}$	Pierrehumbert (1986) Stern et al. (1987) Stern and Pierrehumbert (1988) Alpert et al. (1988)

In addition to the inclusion of the blocking effect, there have been numerous efforts to improve the parameterization of subgrid-scale orographic gravity waves (Table 1). Miller and Palmer (1986) and Miller et al. (1989) introduced directionally dependent subgrid-scale orographic variance. Stern and Pierrehumbert (1988) proposed a scheme that includes the effect of the curvature of vertical wind profile. Surgi (1989) constructed a moist gravity wave drag scheme through the use of a moist Brunt–Väisälä frequency (see also Durran and Klemp 1982a).

Further, Bannon and Yuhas (1990) considered orographic spectral distributions to represent complex terrain instead of subgrid-scale orographic variance. Schoeberl (1988) discussed that supersaturation (Lindzen 1988) occurs as a result of the localization of wave breaking (see also Walterscheid and Schubert 1990) and decreases associated momentum deposition. Kim and Mahrt (1992) generalized the supersaturation hypothesis by including the vertical variation of the mean flow. Bacmeister (1993) explicitly included the effect of orographic anisotropy. Laprise (1993) investigated the validity of the WKBJ approximation in view of the internal reflections and transient effect.

Another important effort to improve the parameterization is made through the inclusion of the effect due to wave breaking at low levels. As discussed earlier by Peltier and Clark (1979), low-level wave breaking occurring in the downstream region may induce a critical layer below which the wave energy is trapped and, consequently, the drag is enhanced through resonant amplification of nonhydrostatic waves. This effect of low-level wave breaking has been neglected in most large-scale models, but its importance is being acknowledged (details will be discussed in section 6).

To date, gravity wave parameterization schemes have been evaluated mainly by comparing results predicted by large-scale models with observations, focusing on the overall improvement of simulated fields. In those results, however, errors from a variety of sources may interact with one another. To avoid this situation, we follow an approach in which parameterization schemes for subgrid-scale orographic gravity waves are evaluated using a mesoscale model that can explicitly simulate gravity waves (Kim and Arakawa 1991):

(i) Regard a subdomain of the gravity wave model as the horizontal grid interval of a large-scale model.

(ii) Use a parameterization scheme to calculate the vertical profile of gravity wave drag from the subdomain-averaged variables.

(iii) Compare the resulting drag profile with the profile of the subdomain-averaged values of the drag simulated by the gravity wave model.

The primary objective of this paper is to investigate the importance of low-level wave breaking and associated drag enhancement in parameterization of subgrid-scale orographic gravity waves. Section 2 introduces the gravity wave model. Section 3 presents numerical simulations of mountain waves with the gravity wave model for various orographic conditions. Section 4 discusses the procedures we use in developing an improved orographic gravity wave parameterization. We first construct a test parameterization scheme based on the existing schemes and evaluate the scheme using the dataset obtained from the mountain wave simulations. We then introduce our scheme, which is revised from the test scheme, and evaluate the revised scheme again using the dataset obtained from the simulations. Section 5 gives a summary of this work. Section 6 discusses the results. Appendix A describes some details of the numerical model, and appendix B defines additional orographic statistical measures of orography.

2. Mesoscale gravity wave model

a. Basic framework

The model is based on the nonhydrostatic anelastic system of equations:

$$\frac{\partial\zeta}{\partial t} = J(\zeta/\rho_0, \psi) + \frac{g}{\theta_0}\frac{\partial\theta}{\partial x} + F_\zeta - L_\zeta\zeta, \quad (2.1)$$

$$\frac{\partial\theta}{\partial t} = \frac{1}{\rho_0} J(\theta, \psi) + F_\theta - L_\theta\theta, \quad (2.2)$$

$$\frac{\partial u}{\partial x} + \frac{1}{\rho_0}\frac{\partial}{\partial z}(\rho_0 w) = 0, \quad (2.3)$$

where x and z are the horizontal and vertical components of Cartesian coordinates, J is the Jacobian operator on the x–z plane, ψ is the streamfunction for the mass flux, ρ is the density, θ is the potential temperature, and the subscript "0" denotes zonally uniform reference states. The vorticity ζ and the x and z components of the wind, u and w, are given by

$$\zeta = \frac{\partial w}{\partial x} - \frac{\partial u}{\partial z}, \quad u = -\frac{1}{\rho_0}\frac{\partial\psi}{\partial z}, \quad w = \frac{1}{\rho_0}\frac{\partial\psi}{\partial x}. \quad (2.4)$$

The terms F_ζ and F_θ represent the effects of turbulence expressed as

$$F_\zeta \equiv -\frac{\partial^2}{\partial x^2}\overline{\overline{u''w''}} - \frac{\partial}{\partial x}\frac{1}{\rho_0}\frac{\partial}{\partial z}\rho_0\overline{\overline{w''w''}} + \frac{\partial}{\partial z}\frac{\partial}{\partial x}\overline{\overline{u''u''}} + \frac{\partial}{\partial z}\frac{1}{\rho_0}\frac{\partial}{\partial z}\rho_0\overline{\overline{u''w''}}, \quad (2.5)$$

and

$$F_\theta \equiv -\frac{1}{C_p\pi_0}\frac{1}{\rho_0}\left(\frac{\partial}{\partial x}\rho_0\overline{\overline{u''s''}} + \frac{\partial}{\partial z}\rho_0\overline{\overline{w''s''}}\right), \quad (2.6)$$

where double overbars and double primes represent the ensemble mean of the three-dimensional turbulence and deviation from the ensemble mean, respectively; $s \equiv C_p\theta\pi_0 + gz$ is the dry static energy, $\pi_0 \equiv (p_0/p_s)^{R/C_p}$ is the reference Exner function, p_s is a characteristic surface pressure, R is the gas constant for dry air, and C_p is the specific heat of dry air at constant pressure. The coefficients, L_ζ and L_θ, are for a thin wave-absorbing sponge layer, which is placed immediately below the upper boundary[2] (see Kim et al. 1993).

The upper-boundary condition requires predicting zonally averaged zonal wind at the boundary. The prediction is through

$$\frac{\partial\bar{u}}{\partial t} = -\frac{1}{\rho_0}\frac{\partial}{\partial z}(\rho_0\overline{u'w'}), \quad (2.7)$$

where the single overbar and single prime denote the zonal mean and the deviation from the zonal mean, respectively. The lateral boundaries of the model are periodic for all variables. The lower boundary of the model consists of rectangular blocks, while the upper boundary is a rigid horizontal surface. The lower-boundary condition with bottom topography is incorporated following Roache (1972) and Pihos and Wurtele (1981).

b. Turbulence parameterization

For the parameterization of the turbulence, we use a combination of the level 1 closure and a prognostic equation for the turbulent kinetic energy, $q^2[\equiv \overline{\overline{(u'')_i^2}}]$, taken from the level 2½ closure model of Mellor and Yamada (1982).

The turbulent kinetic energy equation is written as

$$\frac{\partial q^2}{\partial t} = J(q^2, \psi) + \frac{\partial}{\partial x}\left(\frac{5}{3}q\lambda_1\frac{\partial q^2}{\partial x}\right) + \frac{\partial}{\partial z}\left(\frac{5}{3}q\lambda_1\frac{\partial q^2}{\partial z}\right) - 2\left\{\overline{\overline{u''w''}}\left(\frac{\partial u}{\partial z} + \frac{\partial w}{\partial x}\right) + \overline{\overline{w''w''}}\frac{\partial w}{\partial z} + \overline{\overline{u''u''}}\frac{\partial u}{\partial x} - \frac{g}{\theta_0}\overline{\overline{w''\theta''}} + \frac{q^3}{\Lambda_1}\right\}, \quad (2.8)$$

where $(\lambda_1, \Lambda_1) = (0.23, 16.6)l_m$ and l_m is the master turbulence length scale. Following Mellor and Yamada (1982), we express the parameterized turbulence fluxes as

$$\overline{\overline{u''w''}} = -ql_1\left(\frac{\partial u}{\partial z} + \frac{\partial w}{\partial x}\right), \quad \overline{\overline{w''w''}} = \frac{q^2}{3} - 2ql_1\frac{\partial w}{\partial z},$$

$$\overline{\overline{u''u''}} = \frac{q^2}{3} - 2ql_1\frac{\partial u}{\partial x}, \quad \overline{\overline{u''\theta''}} = -ql_2\frac{\partial\theta}{\partial x},$$

$$\overline{\overline{w''\theta''}} = -ql_2\frac{\partial\theta}{\partial z}, \quad (2.9)$$

where $(l_1, l_2) = (0.92, 0.74)l_m$, while surface turbulence fluxes are calculated by the bulk aerodynamic method. We can rewrite (2.8) by using (2.9) as

$$\frac{\partial q^2}{\partial t} = J(q^2, \psi) + \frac{\partial}{\partial x}\left(\frac{5}{3}q\lambda_1\frac{\partial q^2}{\partial x}\right) + \frac{\partial}{\partial z}\left(\frac{5}{3}q\lambda_1\frac{\partial q^2}{\partial z}\right) + 2ql_1|Def|^2\left(1 - \frac{l_2}{l_1}Ri\right) - \frac{2q^3}{\Lambda_1}, \quad (2.10)$$

---

[2] The system (2.1) and (2.2) with the sponge layer implemented is expressed as

$$\frac{\partial\zeta}{\partial t} = J(\zeta/\rho_0, \Psi) + F_\zeta + \frac{1}{1 + b_s}\frac{g}{\theta_0}\frac{\partial\theta}{\partial x} - \frac{a_s}{1 + b_s}\kappa|\bar{u}|\zeta,$$

$$\frac{\partial\theta}{\partial t} = \frac{1}{\rho_0}J(\theta, \Psi) + F_\theta - \frac{a_s}{1 + b_s}\kappa|\bar{u}|\theta,$$

where a_s (>0) and b_s are functions of vertical grid interval Δz, zonal wavenumber κ (>0), and mean zonal wind $\bar{u}$.

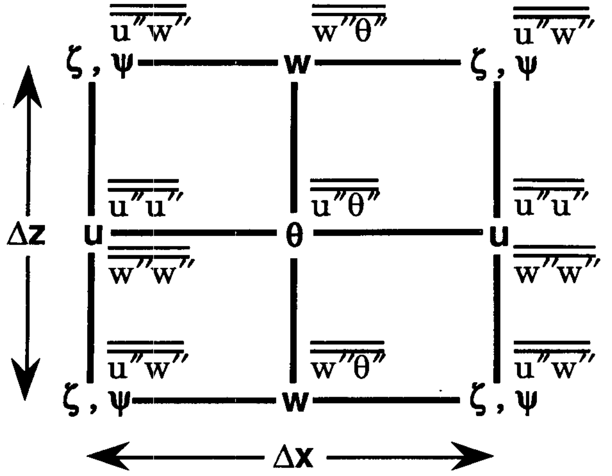

FIG. 1. The distribution of variables on a vertical C grid. Double bars denote ensemble means of the turbulence.

where

$$|Def|^2 \equiv \left(\frac{\partial u}{\partial z} + \frac{\partial w}{\partial x}\right)^2 + 2\left[\left(\frac{\partial u}{\partial x}\right)^2 + \left(\frac{\partial w}{\partial z}\right)^2\right],$$

$$Ri \equiv \frac{\dfrac{g}{\theta_0}\dfrac{\partial \theta}{\partial z}}{|Def|^2}. \quad (2.11)$$

The fourth term in the right-hand side of (2.10) is set to zero if negative. Appendix A describes how we determine l_m.

c. Numerical methods

To solve for streamfunction from vorticity, (2.4) can be combined to give an elliptic equation; that is, $\zeta = (1/\rho_0)\partial^2\psi/\partial x^2 + (\partial/\partial z)[(1/\rho_0)\partial\psi/\partial z]$. In solving this equation for ψ, formally different conditions are applied at the lower and upper boundaries. At the lower boundary, a Dirichlet condition ($\psi = 0$) is used. At the upper boundary, a Neumann condition ($\partial\bar{\psi}/\partial z = -\rho_0\bar{u}$) is applied to the zonal mean part of the streamfunction $\bar{\psi}$ and a Dirichlet condition ($\psi' = 0$) is applied to the deviation part ψ'. Details are given in Kim (1992) and Kim et al. (1993).

In the model, we use a staggered C grid applied to a vertical plane (Fig. 1). For the simulations referred to in section 3a of this paper the grid is stretched vertically following Wilhelmson and Chen (1982), increasing the resolution for the lower part of the model domain. We use the Arakawa Jacobian (Arakawa 1966) for vorticity advection and Takacs' scheme (Takacs 1985) for potential temperature advection and the second-order Adams–Bashforth scheme for time differencing. Details are given in Kim (1992), a summary of which is found in Kim et al. (1993) except for the turbulence terms. The second-order Adams–Bashforth scheme is also used to update vorticity and potential temperature through the turbulence terms F_ζ and F_θ, given by (2.5) and (2.6), respectively. To update turbulent kinetic energy q^2, the backward scheme is used for the dissipation term and partially for the diffusion term in (2.10), while the forward (Euler) scheme is used for the remaining terms.

3. Numerical simulation of mountain waves

a. Comparison of model simulations with analytic solutions

In order to compare model results with corresponding analytic solutions, we use the analyses by Wurtele et al. (1987) for a linear case and Huppert and Miles (1969) for nonlinear cases.

1) COMPARISON WITH THE ANALYSIS BY WURTELE ET AL. (1987)

Wurtele et al. (1987) presented an analytic solution of a two-dimensional linearized stationary Boussinesq system of equations applied to stratified flow in the troposphere, with constant mean vertical wind shear and stability, over a witch of Agnesi terrain.

TABLE 3. Environmental conditions for mountain wave simulations, WSK for a flow over a bell-shaped (witch of Agnesi) barrier by Wurtele et al. (1987), HM# for flows over semielliptical barriers by Huppert and Miles (1969), and ME# for flows over barrier case ME.

Case	Height [m] h	B–V frequency [s^{-1}] N	Mean wind [m s^{-1}] U	Wind shear [s^{-1}] $\Delta U/\Delta z$	Richardson number $Ri \equiv N^2/(\Delta U/\Delta z)^2$	Froude number $Fr \equiv Nh/U$
WSK	100	0.01	10 @ surface	0.0025	16	0.10
HM1	1000	0.01	20	0.0	∞	0.50
HM2	1000	0.01	10.75	0.0	∞	0.93
HM3	1000	0.01	6.66	0.0	∞	1.50
ME	1500	0.01	10	0.0	∞	1.50
ME2	1500	0.015	15	0.0	∞	1.50
ME3	1500	0.02	20	0.0	∞	1.50
ME4	1500	0.005	7.5	0.0	∞	1.00
ME5	1500	0.01	15	0.0	∞	1.00

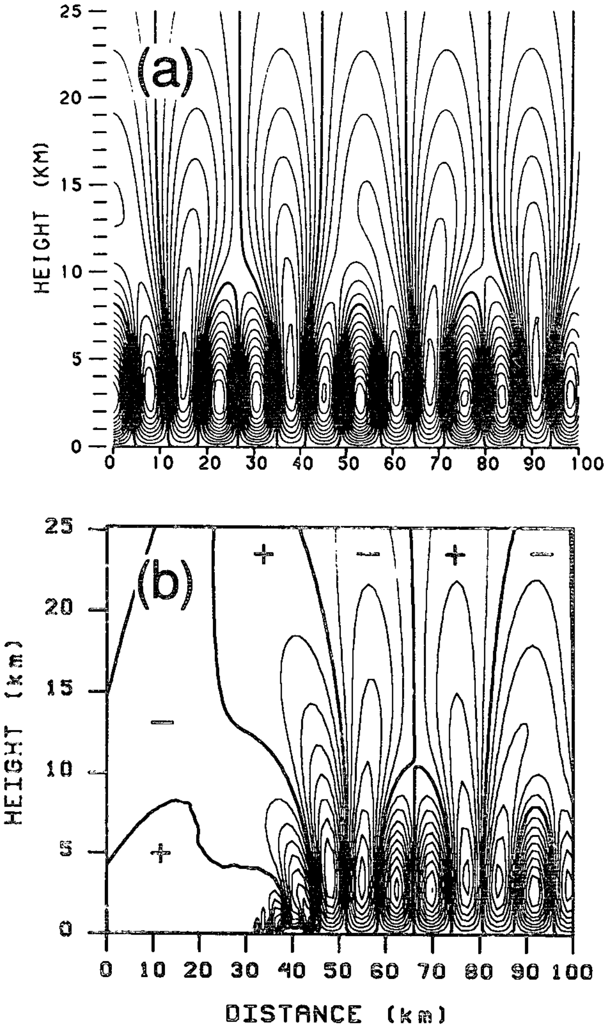

FIG. 2. Vertical velocity fields for case WSK (a) calculated from the linear analysis by Wurtele et al. (1987) and (b) numerically simulated from the Boussinesq version of our model (at 9600 s of model time). For the simulation, $\Delta x = 1250$ m and $\Delta t = 5$ sec. Note, Δz is stretched so that it is 100 and 1330 m for the lowest and highest layers, respectively. The computational domain is 150 km wide and 45.94 km high. The contour interval is 0.2 m s^{-1}, and the heavy contours denote zero lines. (a) The analytic solution represents only a downstream pattern where only the resonant wave remains, while (b) the simulation represents both upstream and downstream patterns.

The analytic solution by Wurtele et al. (1987) and the results from a numerical simulation using the Boussinesq version of our model applied to this case (case WSK, see Table 3) are shown, respectively, in Figs. 2a,b. The turbulence parameterization is shut off in this simulation. From the Froude number at the surface (*Fr* = 0.1), which characterizes mountain waves in view of nonlinearity of the waves, we find that nonlinear effect is not important for this case. Nonhydrostaticity is important, however, due to the vertical wind shear imposed. Although the numerical model used is nonlinear and time dependent, its solution is expected to agree with the analytic solution approximately after it becomes quasi-stationary since nonlinearity is small in this case. Both the analytic solution and simulation show resonantly trapped lee waves propagating downstream. The two resonant waves of different amplitudes (one trapped in the troposphere, the other extended into the stratosphere) are well simulated by our numerical model, showing good qualitative agreement with the analytic solution.

2) COMPARISON WITH THE ANALYSES BY HUPPERT AND MILES (1969)

Huppert and Miles (1969) obtained solutions of stratified Boussinesq flows with constant *N* and *U* over two-dimensional barriers of semielliptical cross sections. We choose three cases from Huppert and Miles (1969) with two different eccentricities of semielliptical barriers.

Figure 3 shows analytic solutions obtained by Huppert and Miles (1969) and numerical simulations from the Boussinesq version of our model for cases HM1 and HM2 (see Table 3). Turbulence is now turned on with no surface fluxes. These cases have the same static stability and barrier. Due to the difference in the mean wind speed, however, the flow characteristics are quite different from each other. Nonlinear effect for case HM1 is small (*Fr* = 0.5), and thus, wave steepening is not expected (see Figs. 3a,b). On the other hand, nonlinear effect for case HM2 is relatively large (*Fr* = 0.93). Thus, wave steepening is simulated (see Figs. 3c,d). The analytic solution for case HM2 is a linear solution for which two regions of wave steepening are

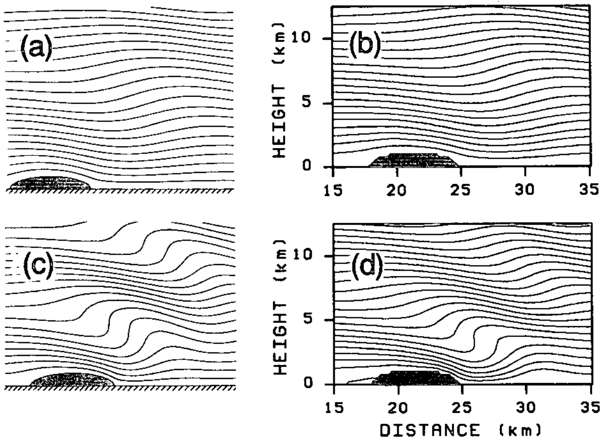

FIG. 3. Streamfunction for flow over a semielliptical barrier. (a) A Boussinesq analytic solution of Huppert and Miles (1969) and (b) a numerical simulation (at 3000 s) from the Boussinesq version of our anelastic model for case HM1 with Fr ($\equiv Nh/U$) = 0.5. For this simulation, $\Delta x = 300$ m, $\Delta z = 250$ m, and $\Delta t = 5$ sec. The computational domain is 75.3 km wide and 35 km high. Panels (c) and (d) are same as (a) and (b) but for case HM2 with $Fr = 0.93$.

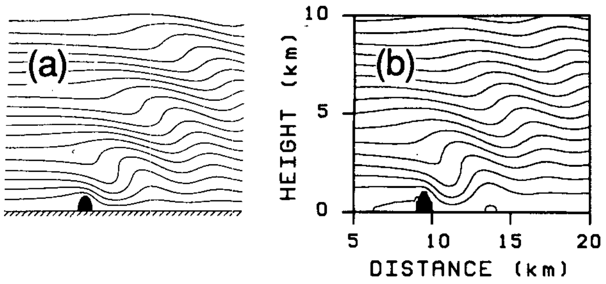

FIG. 4. Streamfunction for flow over a semielliptical barrier for case HM3 with $Fr = 1.5$ from (a) a Boussinesq analytic solution of Huppert and Miles (1969) and (b) a numerical simulation (at 3000 s) from the Boussinesq version of our anelastic model. For this simulation, $\Delta x = 150$ m, $\Delta z = 250$ m, and $\Delta t = 5$ sec. The computational domain is 37.65 km wide and 35 km high.

both assumed to be stationary. In the simulation, a quasi stationary state is approximately reached, first at low levels before the nonlinear effect becomes dominant and later at upper levels, as also shown by Sharman et al. (1988).

Figure 4 shows an analytic solution obtained by Huppert and Miles (1969) and a numerical simulation from the Boussinesq version of the model for case HM3. Nonlinear effect plays a dominant role for this case ($Fr = 1.5$). In the simulation, there is a blocked region of upstream flow due to the steep slope of the block barrier. Also in the simulation, we see a downstream region of isolated flow that seems to be related to a flow separation between the vertically propagating and resonant modes (as discussed by Clark and Peltier 1984). Overall patterns are, however, in good agreement.

b. Simulations with various orography

We performed numerical simulations for various shapes and sizes of mountains. To consider irregularities of real mountains, we designed 35 barriers represented by rectangular blocks to form the lower boundary of the model (see Fig. 5).

1) UPSTREAM FLOW AND MODEL PARAMETERS FOR THE SIMULATIONS

The density and the potential temperature at the surface are 1.225 kg m^{-3} and 288.15 K, respectively. A constant Brunt–Väisälä frequency $N = 0.01$ s^{-1} and a density-scale height $S^{-1} = 9000$ m are used to define the reference states. The mean zonal wind is initialized by $U = 10$ m s^{-1}. The horizontal and vertical grid sizes are 1000 and 500 m, respectively. The integration time interval Δt is 10 sec. The model domain covers 200 km horizontally and 35 km vertically. Turbulence is turned on with no surface fluxes. The value of the master turbulence length scale is about 78 m for the chosen spatial resolutions (see appendix A). The three levels below the top of the model include the sponge designed by Kim et al. (1993).

2) CHARACTERISTICS OF THE SIMULATED FIELDS

We show examples of simulations performed with the same flow parameters but with different barriers. Shown are the snapshots taken when the waves are considered to reach quasi-stationary state. Since waves are slightly transient, we choose the time when the zonally averaged momentum flux at the level immediately above the barrier reaches its first extremum.

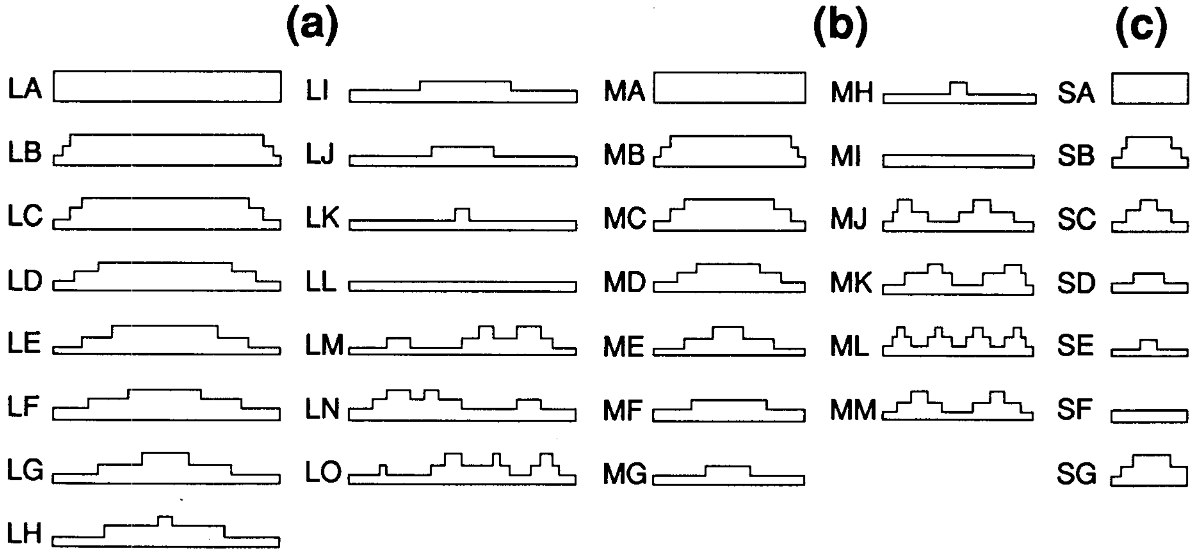

FIG. 5. Barrier cases of various shapes and sizes for (a) large (LX), (b) medium-sized (MX), and (c) small (SX) barriers. Cases LM, LO, MK, and SG are asymmetric barriers with gentle upslope and steep downslope to generate strongly nonlinear waves (e.g., Lilly and Klemp 1979). Cases LN and MJ are mirror images of cases LM and MK, respectively.

Wave breaking occurs when *Fr* is greater than its critical value ($Fr_c = 1$ in this study, see Fig. 6). The region of wave breaking is well characterized by local steepening of the potential temperature fields. Usually, this region is associated with a local reversal of the cross-mountain flow inducing a nonlinear critical layer as shown by thick solid contours for the zonal velocity fields. The overall look of the simulated flows with low-level wave breaking (e.g., case LO) seems to resemble that of the hydraulic theory, which has been

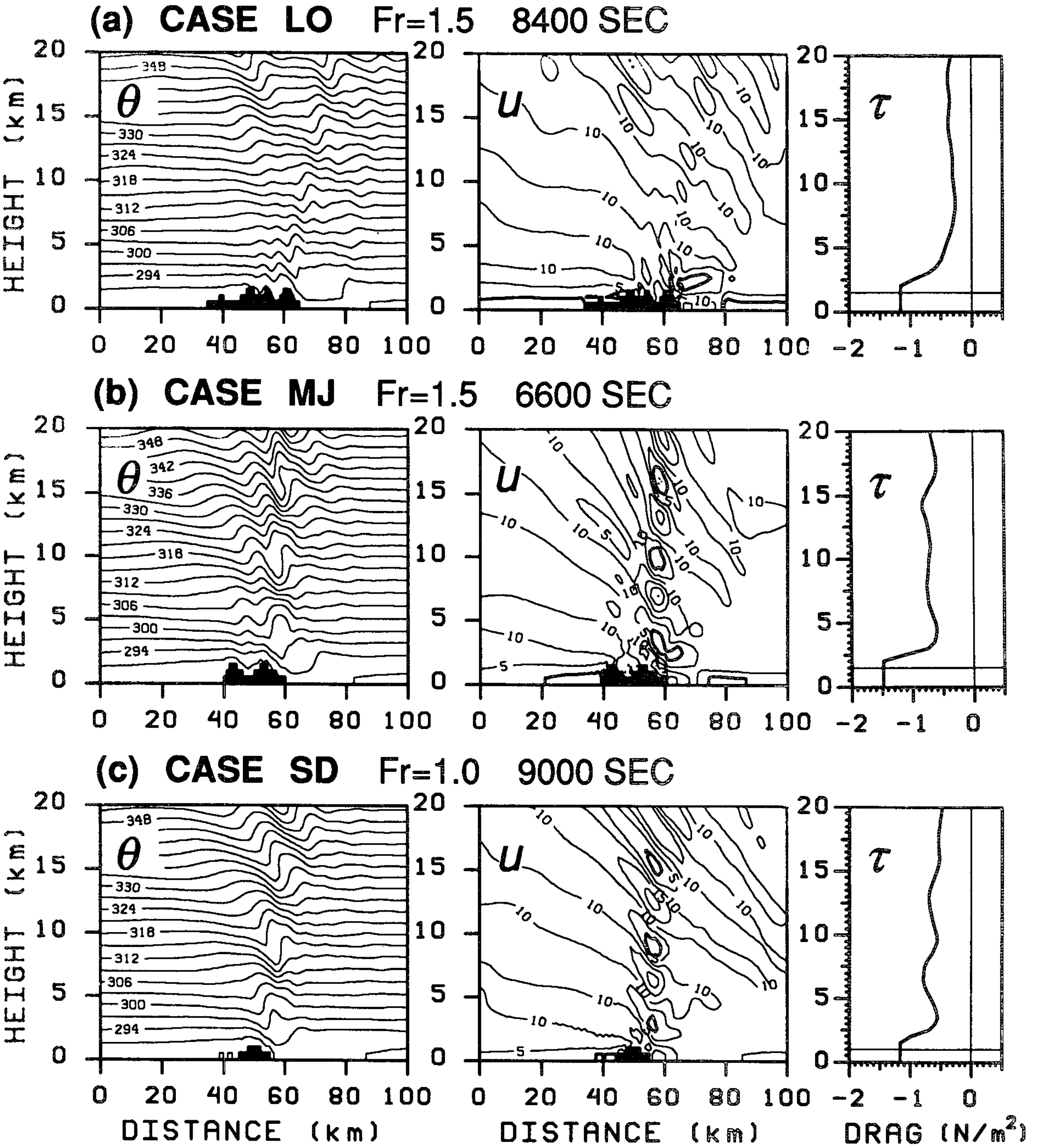

FIG. 6. Simulated mountain waves for cases (a) LO ($Fr = 1.5$), (b) MJ ($Fr = 1.5$), and (c) SD ($Fr = 1.0$). From left, fields of the potential temperature θ (K), zonal velocity u (m s^{-1}), and horizontal domain average of vertical momentum flux (drag) τ (N m^{-2}) are shown. The reference level is shown by the thin horizontal line in the drag profile. Ignore the drag profile below the reference level.

successfully applied to explaining large-amplitude mountain waves (Smith 1985; Durran 1986; Durran and Klemp 1987). Vertically propagating waves may be reflected from the wave-breaking region and resonantly amplified, enhancing the divergence of vertical momentum flux as discussed by Peltier and Clark (1979, 1983) and Clark and Peltier (1984).

It is also noted that upstream flow blocking, which is characterized by a stagnant upstream low-level flow, occurs when Fr is relatively large (see the zonal velocity fields). Another stagnant region is found near the surface far downstream off the barriers (e.g., case MJ), which may be associated with a hydraulic jump.

4. Parameterization of orographic gravity waves

a. Assessment of a test parameterization scheme for orographic gravity wave drag

1) A TEST PARAMETERIZATION SCHEME

We construct a test parameterization scheme by adopting some essential features of the existing schemes. The reference-level drag is determined using the formulation by Pierrehumbert (1986), while the vertical distribution of drag is obtained following the algorithm by Miller and Palmer (1986), which incorporates the wave saturation hypothesis by Lindzen (1981) and the Eliassen–Palm theorem (Eliassen and Palm 1960). An outline of the test scheme is given in Table 1 together with those of selected existing schemes.

The reference-level drag is commonly expressed (e.g., Palmer et al. 1986) as

$$\tau_0 = k\rho_0 N_0 U_0 h^2, \tag{4.1}$$

where the subscript "0" stands for the reference level; k is a tunable coefficient; U_0 and N_0 are the low-level wind component in the direction of reference-level drag and the low-level Brunt–Väisälä frequency, respectively; and h is a height proportional to the standard deviation of sub-grid-scale orographic height. For the treatment of nonlinear effect resulting from a large Froude number at the reference level, Fr_0 $(\equiv N_0 SD/U_0)$, Pierrehumbert (1986) expressed the reference-level drag, instead of (4.1), as

$$\tau_0 = \frac{m}{\Delta x}\frac{\rho_0 U_0^3}{N_0} G, \qquad (4.2)^3$$

where m $(<\Delta x/L_m$, Δx is the grid interval and L_m is the mountain width) is the number of (sub-grid-scale) mountains in a grid interval and

$$G \equiv G_{\max}\frac{Fr_0^2}{Fr_0^2 + a^2}. \tag{4.3}$$

Here, $G_{\max}$ is a nondimensional saturation flux (set to 1 in this study as is usually done) and a is a function of the mountain-aspect ratio[4] (also set to 1).

The drag above the reference level can be expressed similarly to (4.1) as

$$\tau = \frac{m}{\Delta x}\rho N U h_d^2, \tag{4.4}$$

where h_d is the displacement wave amplitude. In the absence of wave breaking, the displacement amplitude for the ith layer can be expressed using the drag for the layer immediately below. Thus, assuming $\tau_i = \tau_{i+1}$, (4.4) is rewritten as

$$h_{d_i}^2 = \frac{\Delta x}{m}\frac{\tau_{i+1}}{\rho_i N_i U_i}. \tag{4.5}$$

The minimum Richardson number or local wave-modified Richardson number, which determines the onset of wave breaking, is expressed in terms of Ri and Fr_d $(=Nh_d/U)$ based on zonal mean N^2 and U:

$$Ri_m = \frac{Ri(1 - Fr_d)}{(1 + \sqrt{Ri}\cdot Fr_d)^2}. \tag{4.6}$$

Wave breaking occurs when $Ri_m < Ri_c$ $(=0.25)$. Then Lindzen's wave saturation hypothesis resets the displacement amplitude h_d to that corresponding to $Ri_m = 0.25$. Substituting $Ri_m = 0.25$ in (4.6), we obtain the critical h_d (or h_c) expressed in terms of the mean values of U, N, and Ri:

$$h_c = \frac{U}{N}\left\{2\left(2 + \frac{1}{\sqrt{Ri}}\right)^{1/2} - \left(2 + \frac{1}{\sqrt{Ri}}\right)\right\}. \tag{4.7}$$

We determine the vertical profile of the orographic Reynolds stress (or drag) as follows. (i) Calculate τ_0 from (4.2). (ii) Compute h_d from (4.5). (iii) Check the stability by using h_d in (4.6). If $Ri_m \leqslant Ri_c$, obtain τ from (4.4) by using h_c computed from (4.7); otherwise τ is unchanged. (iv) Repeat steps (ii) and (iii) at the next level unless either τ approaches zero or the model top is reached.

2) ASSESSMENT OF PARAMETERIZATION SCHEMES USING THE DATASET OBTAINED FROM MOUNTAIN WAVE SIMULATIONS

When extracting statistics from the dataset obtained from the mountain wave simulations, we take the temporal average of the fields for the interval of 1 h centered at the time of the first extremum of the zonally

---

[3] Similar to (4.1) with SD $\leqslant$ 400 m (Palmer et al. 1986) in terms of the magnitude of τ_0, but provides smoother transition between blocking and nonblocking flows. [For small Fr_0, (4.2) reduces to (4.1) with $m/\Delta x \approx k$.]

[4] $AR \equiv h/a$, the ratio of the height to the half-width of the mountain.

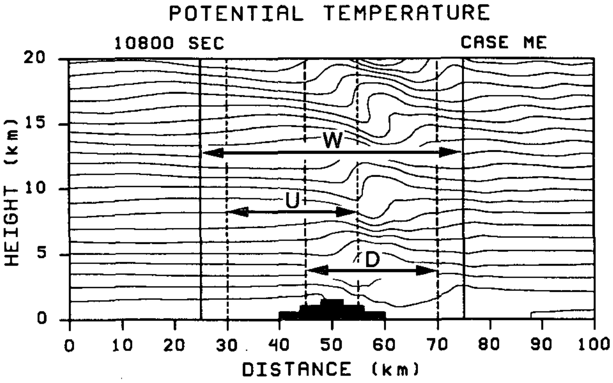

Fig. 7. Simulated potential temperature for case ME. The domain is divided into three subdomains for application of parameterization schemes: W (x = 25–75 km, solid lines), U (30–55 km, short dashed lines), and D (45–70 km, long dashed lines).

averaged momentum flux at the reference level. This process is expected to eliminate short-term transience.

We note that an improper estimation of low-level drag may lead to under- or overestimation of the intensity of upper-level drag divergence. In some large-scale models, the reference level is raised very high, well above the lower troposphere, to avoid the difficulty in parameterizing low-level drag and concentrate on parameterizing upper-level drag. Moreover, some use arbitrarily increased values of SD for tuning τ_0. We try to reproduce these situations of the existing parameterization schemes in our experiments.

We carry out a series of experiments by applying our test parameterization scheme to the dataset. We create situations with low-level wave breaking, such as case ME ($Fr = 1.5$) shown in Fig. 7. We choose $m = 2.5$ as the basic value following Pierrehumbert's (1986) criteria applied to this case (i.e., $m < \Delta x / L_m = 50$ km/20 km). The calculated value of k ($= m/\Delta x$) is 5×10^{-5} m^{-1}, which has the same order of magnitude as the value 2.5×10^{-5} m^{-1} used by Palmer et al. (1986) and many others.

Figure 8 compares, for subdomain W (from $x = 25$ to 75 km), the drag profiles explicitly simulated by the numerical gravity wave model (solid line) and those obtained from the test parameterization scheme (dashed line) for certain choices of m (equivalently, k), the reference level, and SD. First of all, we find that increasing m helps improve the reference-level drag (compare the top panels of Fig. 8). This is no longer true, however, for the drag divergence at low levels, which is important for the parameterization. Except near the top, the scheme does not detect any wave dissipation for this case. Second, we find that varying the height of the reference level, with m fixed, does not significantly change both the intensity of the drag and its divergence (compare the middle panels with Fig. 8b). Next, with m and the height of the reference level fixed, increasing SD improves the result to some extent (compare the bottom panels with Fig. 8a). Drag divergence at low levels, however, is still very weak—even with the largest value[5] of SD we tested as shown in Fig. 8i. Moreover, it is difficult to determine the necessary amount of increase in SD.

We also perform tuning experiments with some standard existing schemes, such as those by Palmer et al. (1986), Miller and Palmer (1986), and McFarlane (1987), which are outlined in Table 1 (see also Table 2). Figure 9 shows the results for case ME with the scheme of Palmer et al. (1986), which is comparable to Fig. 8 except that Figs. 9g–i are the results without the limit on SD (i.e., SD $\leqslant$ 400 m) but with different m. Figure 10 shows the results with Miller and Palmer's scheme (panels a–f) and those with McFarlane's formulation to treat the blocking effect (panels g–i). Comparison of these figures with Fig. 8 (panels a–f) shows that the test scheme (a hybrid scheme) performs similarly to these schemes, at least for case ME. The performance of the test scheme is particularly similar to that of Palmer et al., which is widely used in large-scale models. We thus continue to use our test scheme as the base scheme in this study.

Despite tuning as shown above for case ME, the low-level drag divergence is either not produced or seriously underestimated by the test parameterization scheme. Through experiments with other cases, we found that this is a general tendency. Figures 9g–i demonstrate that relaxing the limit on SD enhances the magnitude of the reference-level drag but does not necessarily enhance the divergence at low levels. Since low-level wave breaking occurs mainly in downstream regions, we perform a more detailed analysis to see more local behavior of the test scheme. We consider two more subdomains (see Fig. 7)[6], U (from $x = 30$ to 55 km) and D (from 45 to 70 km), as well as subdomain W used earlier. In determining a single statistical value of k, which is needed in applying the scheme, we first consider the three barrier widths (L, M, and S; see Fig. 5) together with the three subdomains defined above. We then take the average of m for the three barrier widths for each subdomain (see Table 4). We adjust $\bar{m}$ in such a way that k ($= \bar{m}/\Delta x$) has a fixed value regardless of the subdomains, as in most existing parameterization schemes. The resulting

---

[5] Note that the effect of increasing SD in (4.2) is a fraction of that with (4.1) due to the asymptotic nature of function G.

[6] When the interval for which the horizontal average is taken is not a multiple of the wavelengths of the waves, wiggles appear in the profiles of momentum flux. This phenomenon will become more noticeable as the horizontal grid size of large-scale models becomes shorter since the Eliassen–Palm theorem tends to become less applicable. To reduce undesired effects of this situation, it may be useful to horizontally smooth the output from a parameterization scheme over a few grid intervals.

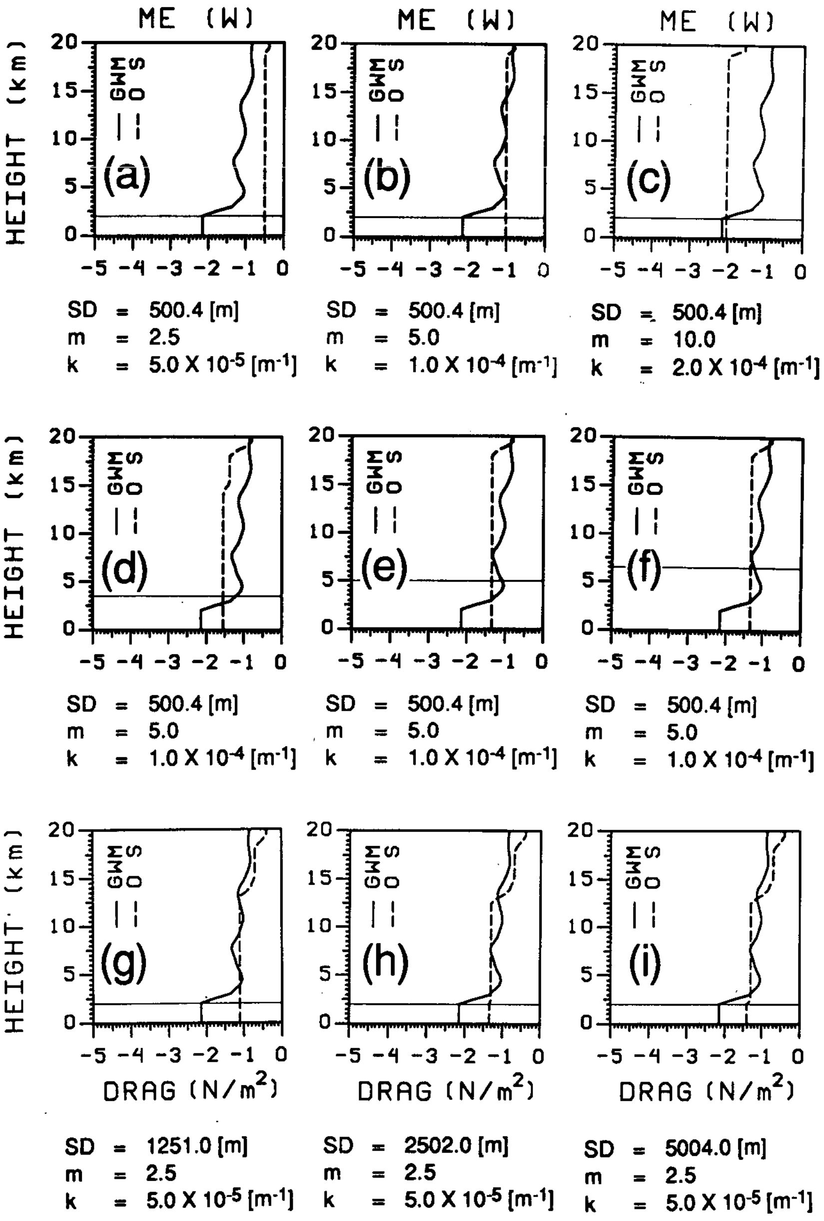

(a) SD = 500.4 [m]
m = 2.5
k = 5.0 X 10^{-5} [m^{-1}]

(b) SD = 500.4 [m]
m = 5.0
k = 1.0 X 10^{-4} [m^{-1}]

(c) SD = 500.4 [m]
m = 10.0
k = 2.0 X 10^{-4} [m^{-1}]

(d) SD = 500.4 [m]
m = 5.0
k = 1.0 X 10^{-4} [m^{-1}]

(e) SD = 500.4 [m]
m = 5.0
k = 1.0 X 10^{-4} [m^{-1}]

(f) SD = 500.4 [m]
m = 5.0
k = 1.0 X 10^{-4} [m^{-1}]

(g) SD = 1251.0 [m]
m = 2.5
k = 5.0 X 10^{-5} [m^{-1}]

(h) SD = 2502.0 [m]
m = 2.5
k = 5.0 X 10^{-5} [m^{-1}]

(i) SD = 5004.0 [m]
m = 2.5
k = 5.0 X 10^{-5} [m^{-1}]

FIG. 8. Sensitivities of the drag for case ME to choices of the number of mountains (*m*), the reference level, and SD. The drag profile drawn by solid line is from the gravity wave model and that by dashed line is from the parameterization scheme.

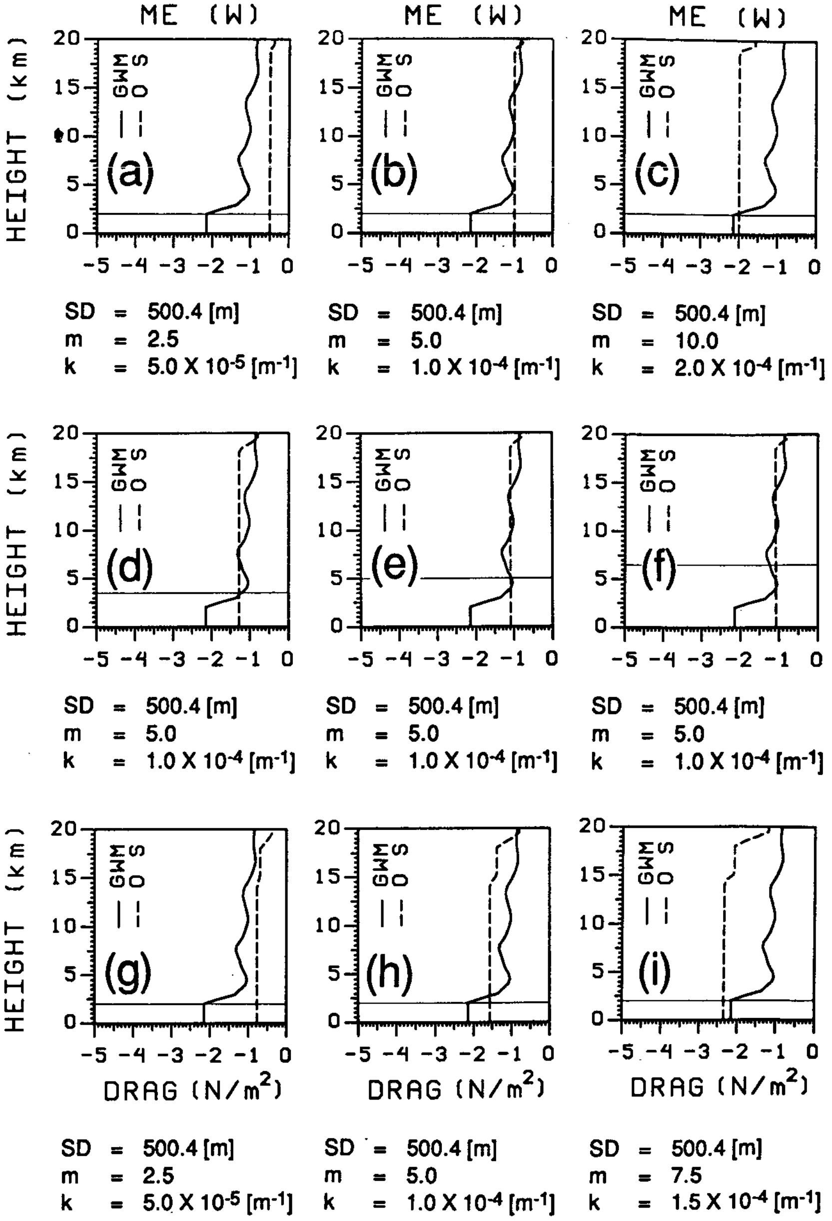

(a) SD = 500.4 [m]
m = 2.5
k = 5.0 X 10^{-5} [m^{-1}]

(b) SD = 500.4 [m]
m = 5.0
k = 1.0 X 10^{-4} [m^{-1}]

(c) SD = 500.4 [m]
m = 10.0
k = 2.0 X 10^{-4} [m^{-1}]

(d) SD = 500.4 [m]
m = 5.0
k = 1.0 X 10^{-4} [m^{-1}]

(e) SD = 500.4 [m]
m = 5.0
k = 1.0 X 10^{-4} [m^{-1}]

(f) SD = 500.4 [m]
m = 5.0
k = 1.0 X 10^{-4} [m^{-1}]

(g) SD = 500.4 [m]
m = 2.5
k = 5.0 X 10^{-5} [m^{-1}]

(h) SD = 500.4 [m]
m = 5.0
k = 1.0 X 10^{-4} [m^{-1}]

(i) SD = 500.4 [m]
m = 7.5
k = 1.5 X 10^{-4} [m^{-1}]

FIG. 9. As in Fig. 8 but with scheme of Palmer et al. (1986). Panels (g)–(i) are without imposing the limit on SD (≤400 m).

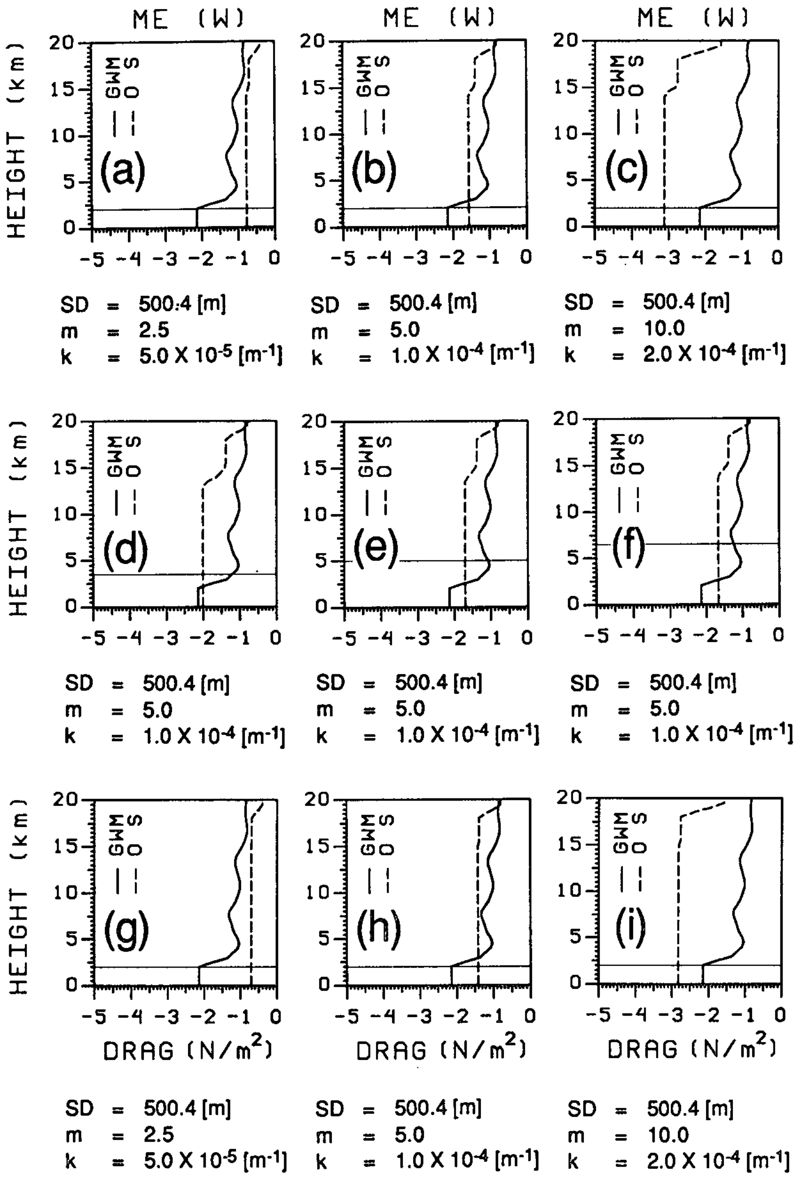

FIG. 10. As in Fig. 9 but (a)–(f) with scheme of Miller and Palmer (1986) and (g)–(i) with formulation from McFarlane (1987) for the reference-level drag.

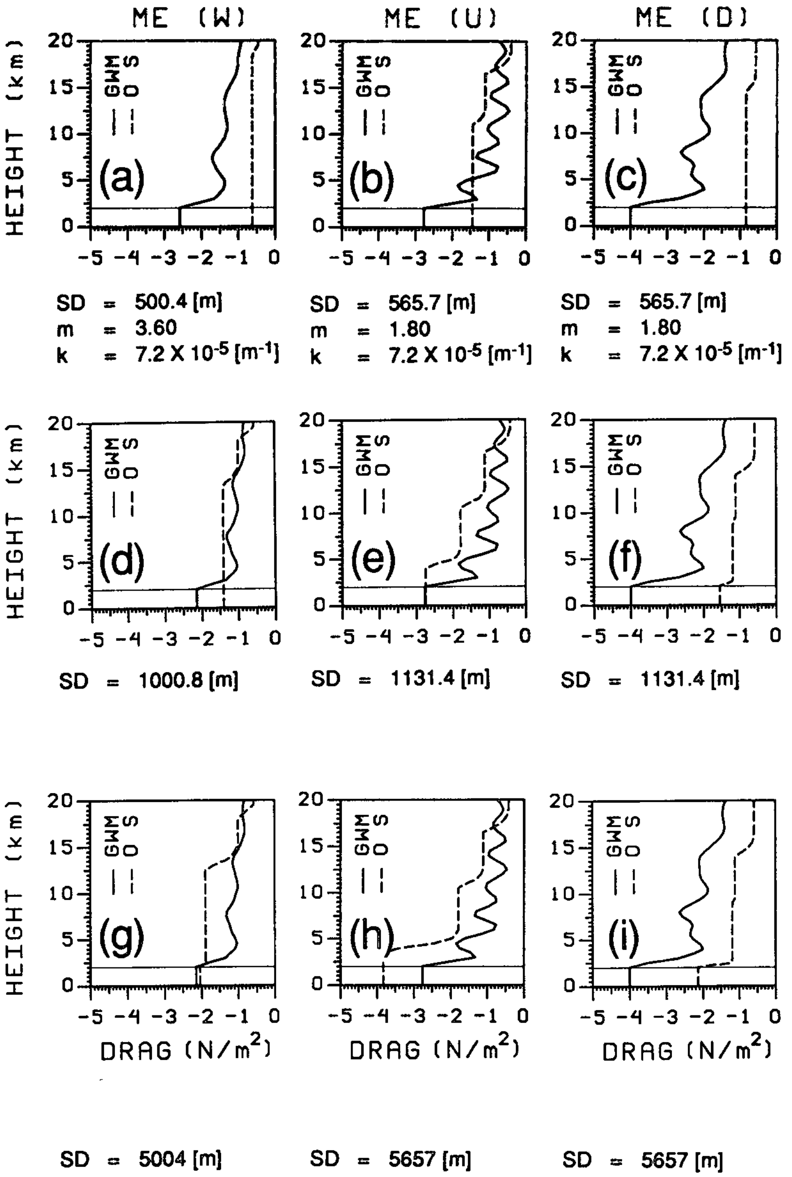

FIG. 11. Comparison of the drag profiles from the gravity wave model (solid line) and from the parameterization scheme (dashed line) for subdomains of case ME shown in Fig. 7. The upper panels are with the original values of SD and m. The middle and the lower panels are as the upper panels, except with 2- and 10-times larger values of SD, respectively.

TABLE 4. Determination of the number of sub-grid-scale mountains *m* following Pierrehumbert (1986) for barrier widths *L*, *M*, and *S*, and for subdomains *W*, *U*, and *D*.

Barrier size	L		M		S	
Subdomain	W	U/D	W	U/D	W	U/D
Δx [km]	50	25	50	25	50	25
L_m [km]	30	20	20	15	10	10
$m = \Delta x/L_m$	1.67	1.25	2.50	1.67	5.00	2.50

k is 7.2×10^{-5} m^{-1}, and the corresponding $\bar{m}$ is 3.6 and 1.8 for W and U/D, respectively.

Figure 11 compares the results of applying the scheme to case ME. The upper three panels are the results with the original values of SD and m calculated above. The overall difference between the profiles of model-simulated drag and scheme-parameterized drag is largest for subdomain D at low levels, indicating that low-level wave breaking occurring in the downstream region is not well parameterized. The middle panels of Fig. 11 show the results with the doubled values of SD. We see that the increase of SD significantly improves the result for the subdomain U but not much for the subdomain D. The lower panels of Fig. 11, which are the results with a 10-times larger SD, show that further increase of SD can result in overestimation of the drag and its divergence for subdomain U; whereas, it improves the result for subdomain D. We found similar results with other cases.

Based on our experiments and analyses, we summarize the weakness of the test parameterization scheme as follows:

- The parameter m (or equivalently the coefficient k) and SD are generally not sufficient to tune the magnitude of the reference-level drag and the drag divergence at low levels.
- The parameterization at low levels can be improved by tuning SD for regions without breaking waves and not for regions with breaking waves.

In conclusion, our results suggest that the effect of low-level wave breaking—that is, enhancement of low-level drag—is not properly included in the test scheme. We believe that this situation is more or less common among the existing schemes.

In terms of SD, which is the only statistical information other than k regarding the orography in the test scheme, subdomains U and D are indistinguishable because they contain the antisymmetric portions of the barrier (see Fig. 7). Consequently, even with the same barrier in the domain, the validity of the scheme depends on the choice of the grid location relative to the barrier. To distinguish between these cases, we believe that additional statistical information on orography other than the standard deviation is needed. This motivates us to move our attention to more detailed information on orography, that is, higher moments of orographic statistics.

3) THE SCORER PARAMETER AND THE NONLINEAR DRAG ENHANCEMENT

The Scorer parameter[7] determines the vertical wavenumber of waves. Weissbluth and Cotton (1989) related locally large values of the Scorer parameter (Scorer 1949), which are due to local flow deceleration, to wave breaking. Durran (1986, 1990) discussed the development of large-amplitude mountain waves and the corresponding increase of the chances for wave breaking due to Scorer parameter layering, in which the variables of a layered atmosphere are structured in such a way that the Scorer parameter changes with height. Iwasaki et al. (1989) pointed out the potential usefulness of including the vertical profile of the Scorer parameter in parameterizing short nonhydrostatic waves that are accompanied by a large amount of vertical momentum transfer.

We find that there is a rapid drop of the Scorer parameter near the reference level for subdomain D (see Fig. 12). This is associated with a local nonlinear critical layer formed near the reference level within this subdomain. Nonhydrostatic gravity waves can then be resonantly amplified near the reference level, enhancing low-level drag and its divergence as discussed in section 3b. In fact, comparison of Figs. 11 and 12 suggests that the low-level drag divergence is closely related to the decrease of the Scorer parameter with height. We believe that this resemblance between the vertical drag divergence and the Scorer parameter decrease, which is also common in other wave-breaking cases we have studied, can be used in the parameterization. The region of low-level wave breaking, however, generally occupies only a portion of the grid interval of large-scale models. Thus, it is difficult to detect the existence of a local nonlinear critical layer induced by the waves from the grid-scale variables. Therefore, we follow an indirect way in which we introduce additional statistical measures of sub-grid-scale orography that are directly related to the existence of the nonlinear critical layer.

b. Revision of the test parameterization scheme

1) THE FROUDE NUMBER AND THE SCORER PARAMETER FOR THE PARAMETERIZATION

One of the distinguishing features among the existing parameterization schemes is the method of treating the upstream flow blocking phenomenon. Some of the criteria for the flow blocking use ad hoc cutoff limits on SD, while some use the relationship between SD, N and U, or their combination in terms of the Froude

---

[7] For our anelastic system, it is defined as $l^2 \equiv N^2/U^2 - S^2/4 - \gamma/U$, where the buoyancy N, the heterogeneity S, and the vertical wind curvature γ are defined by $N^2 \equiv (g/\theta_0)(d\overline{\theta}/dz)$, $S \equiv -d\ \ln\rho_0(z)/dz$, and $\gamma \equiv -\rho_0(d/dz)(\overline{\zeta}/\rho_0) = \rho_0(d/dz)[(1/\rho_0)(dU/dz)]$, respectively.

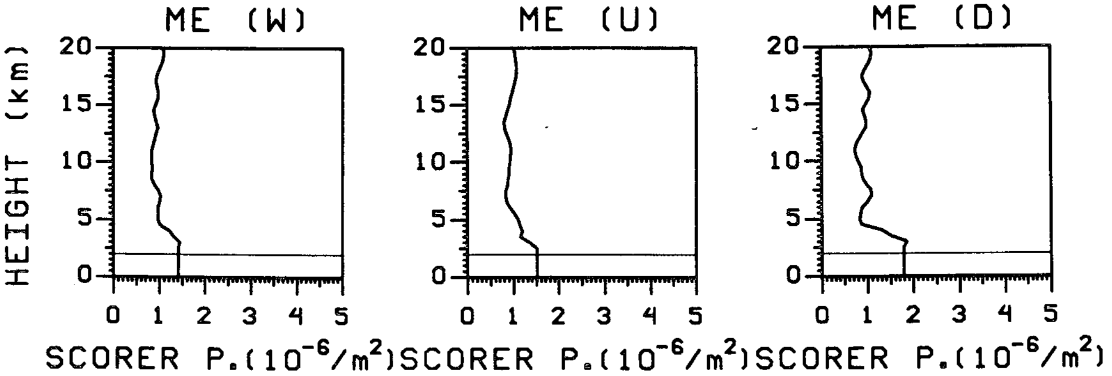

FIG. 12. Comparison of the profiles of the Scorer parameter for the three subdomains.

number ($Fr \equiv N*\mathrm{SD}/U$) as given in Table 2. These criteria, however, affect not only the upstream region but also the downstream region if the two regions are not treated separately. The downstream region, which is accompanied not by flow blocking but by low-level wave breaking, is improperly governed by the flow-blocking criteria, which are originally designed to treat the upstream region only.

We investigate how the Froude number at the reference level, Fr_0, can represent the effect of low-level wave breaking by analyzing the dataset obtained from the gravity wave model. We consider subdomains U and D for the upstream and downstream regions (Fig. 7). We use the deviation of the Scorer parameter at the reference level from that of the vertical environment (2.5 km above the reference level) as a measure of the magnitude of drag enhancement due to low-level wave breaking. Figure 13 shows that Fr_0 is relatively well correlated with the deviation Δl^2 for each subdomain. When the two subdomains are combined, however, Δl^2 cannot be uniquely determined from Fr_0 only. That is, the (domain averaged) Froude number alone, which measures the nonlinearity of averaged flow, is not effective in representing low-level wave breaking that occurs due to strong local nonlinearity of flow. We thus devise a better parameter to represent Δl^2 than Fr_0 alone by introducing additional statistical measures of orography and combining them.

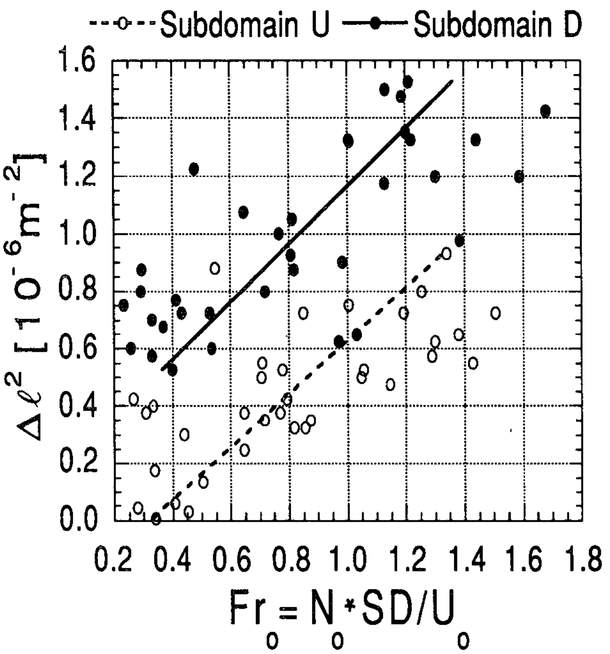

FIG. 13. Scatter plots of the deviation of the Scorer parameter (Δl^2) at the reference level from that at 2.5 km above vs the Froude number at the reference level (Fr_0) for subdomain U (denoted by open circles and dashed line) and subdomain D (denoted by dots and solid line) shown in Fig. 7. For each subdomain, statistics are obtained from 35 mountain wave simulations.

2) ADDITIONAL STATISTICAL MEASURES OF OROGRAPHY

Besides the mean ($\bar{h}$) and SD of orographic height, we devised the orographic asymmetry and convexity parameters (abbreviated as OA and OC, respectively), which statistically determine, respectively, how skewed (asymmetric) and how protruded (sharp) the sub-grid-scale orography is for a grid interval of a large-scale model. Figure 14 schematically illustrates the definitions of OA and OC, and Fig. 15 shows the values of OA and OC for case ME (see appendix B for details).

The value of OA takes into account the relative asymmetry of orography with respect to the center of the domain under consideration; OC is designed as a parameter for multiple irregular barriers, which reduces to mountain aspect ratio (AR) for single symmetric barriers (see Fig. 16). From the values of SD, OA, and OC for this case, we see that OA serves as a measure for distinguishing between subdomains U and D.

3) THE REVISED SCHEME

We formulate the reference-level drag as

$$\tau_0 = E\frac{m'}{\Delta x}\frac{\rho_0 U_0^3}{N_0}G', \tag{4.8}$$

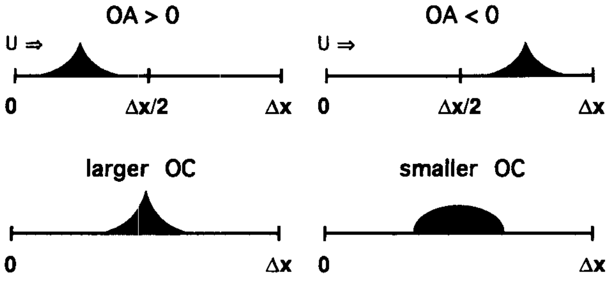

FIG. 14. Illustration of (a) Orographic Asymmetry and (b) Orographic Convexity defined in appendix B. In case of an isolated single symmetric barrier, OA is positive (negative) if the barrier is located toward the upwind (downwind) direction and is zero if the barrier is located in the center of a domain. Sharper (duller) barrier yields a larger (smaller) value of OC.

where E, m', and G' are an enhancement factor, the "number of mountains," and a flux function to be specified, respectively. Here, primes denote revised expressions to be distinguished from those of the test scheme, given by (4.2)–(4.5), hereafter called the original scheme. The drag above the reference level is identical in form to (4.4) except that m is replaced by m'.

We define m' and E in such a way that they depend on the geometry and location of the subgrid-scale orography through OA and the nonlinearity of flow above the orography through Fr. We include OC in the saturation flux G' in such a way that G' is proportional to OC (to be discussed later). The forms of E, m', and G' we have chosen are

$$E(\mathrm{OA}, Fr_0) = (\mathrm{OA} + 2)^{\delta}; \quad \delta = C_E Fr_0/Fr_c, \tag{4.9}$$

$$m'(\mathrm{OA}, L_h) = C_m \Delta x \Big(1 + \sum_x L_h/\Delta x\Big)^{\mathrm{OA}+1}, \tag{4.10}$$

$$G'(\mathrm{OC}, Fr_0) = \frac{Fr_0^2}{Fr_0^2 + a^2}; \quad a^2 = C_G \mathrm{OC}^{-1}, \tag{4.11}$$

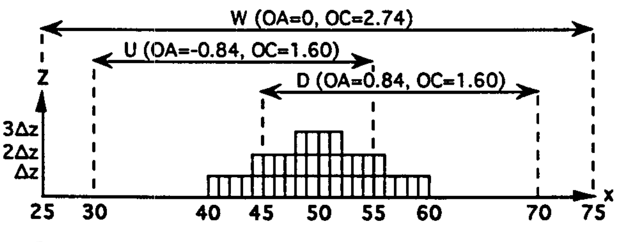

FIG. 15. Configuration of case ME represented by rectangular blocks and corresponding values of OA and OC for the three subdomains. Bold type numbers denote the horizontal grid index. The orographic statistics depend upon the relative location of the barrier in the domain as well as the sizes of the barrier and domain.

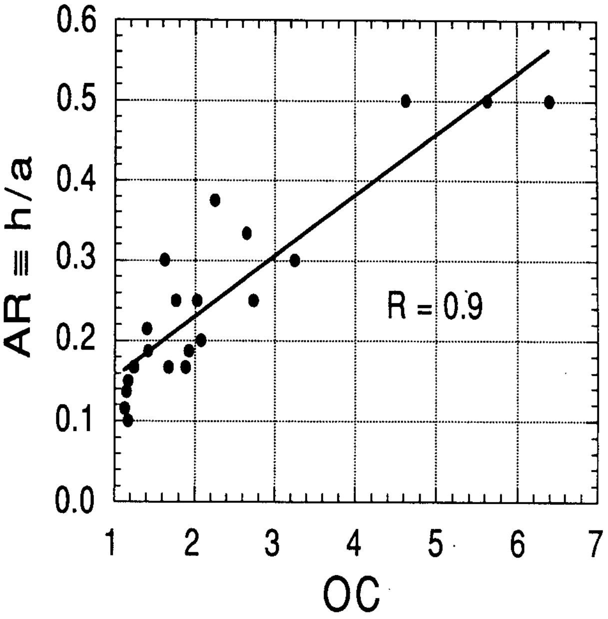

FIG. 16. Scatter plot of the OC vs the AR of the barrier. Statistics are obtained from 21 symmetric single barriers shown in Fig. 5, excluding the flat rectangular barriers. To approximately determine the barrier half-width, we measure the width from the horizontal center of each barrier to a point on the barrier at which the mean height of the barrier intersects. The correlation between AR and OC is 0.9.

where Fr_C (=1) is the critical Froude number, L_h is the width of a horizontal cross section of orography at the critical height defined by $h_C \equiv Fr_C U_0/N_0 = \mathrm{SD}*Fr_C/Fr_0$ (see Fig. 17), $\Sigma_x L_h/\Delta x$ ($\equiv L_x$) is the fractional width covered by the subgrid-scale orography higher than h_C for a domain with the interval Δx, and C_E, C_m, and C_G are constants to be specified.

We set δ as proportional to Fr_0 to avoid excessive enhancement of the reference-level drag when the flow is not strongly nonlinear. The factor OA for m' is used in such a way that the magnitude of the enhancement

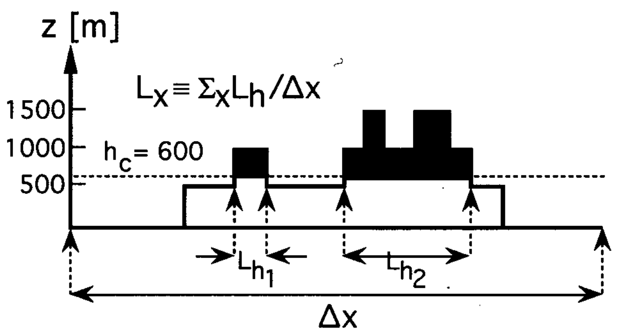

FIG. 17. Determination of L_x (the fractional area covered by the critical sub-grid-scale orography) depending upon the nonlinearity of the flow for case LM. Smaller h_c represents stronger nonlinear flow with larger Fr_0.

depends on the location of the barrier. Note that large m (in the original scheme) does not necessarily promote wave breaking at low levels[8] (see Figs. 9g–i). Therefore, we introduce the additional factor E, which enhances only the reference-level drag, while through parameter m' we control both the drag at the reference level and its divergence above the reference level.

In this study, we set $C_E = 0.8$, $C_m = 3.3 \times 10^{-5}\ \mathrm{m}^{-1}$, and $C_G = 0.5$. With typical values of parameters,[9] $E = 1$ and $m' = 1$ (no enhancement) for typical upstream configuration, while for typical downstream configuration they give $E = 3$ and $m' = 4$. (This magnitude of the enhancement is comparable to that of strongly nonlinear mountain waves based on numerical simulations.) An advantage of using m' and E can be seen in Fig. 18, which shows that Δl^2 is now almost uniquely determined from m' and E. This is in contrast to Fig. 13, in which Fr_0 is used instead, indicating that m' and E can better parameterize the effect of resonant nonhydrostatic waves than Fr_0 alone.

From a series of experiments, we found that the magnitude of drag divergence tends to be underestimated by the revised scheme in low-level downstream regions with wave breaking. Therefore, at low levels when OA > 0 (i.e., in the "downstream" region) we tentatively replace the saturation hypothesis by the following formula based on the ratio of the Scorer parameter:

$$\frac{\tau_i}{\tau_{i+1}} = \mathrm{Min}\left[C_l \frac{l_i^2}{l_{i+1}^2},\ 1 \right], \qquad (4.12)$$

below 10 km, where $C_l = 1$ and l^2 is calculated from the input to the scheme.

4) ASSESSMENT OF THE REVISED PARAMETERIZATION SCHEME FOR DOMAINS CONTAINING A SINGLE SIMPLY SHAPED BARRIER

We again analyze case ME (Fig. 7). Figure 19 compares the drag profiles obtained from the gravity wave model (solid line) with those parameterized by the original scheme (long dashed line) and by the revised scheme (short dashed line). We compare the results for subdomains U and D. For subdomain U, the value of Ek' ($\equiv Em'/\Delta x = 3.8 \times 10^{-5}\ \mathrm{m}^{-1}$) is smaller than k ($=7.2 \times 10^{-5}\ \mathrm{m}^{-1}$), while G' ($=0.66$) is larger than G ($=0.37$). The two schemes provide similar magnitudes of the reference-level drag ($Ek'G'/kG = 0.94$). The revised scheme, however, produces drag divergence at low levels. For subdomain D, Ek' ($=1.3 \times 10^{-4}\ \mathrm{m}^{-1}$) is much larger than k ($=7.2 \times 10^{-5}\ \mathrm{m}^{-1}$), while G' ($=0.67$) is moderately larger than G ($=0.39$). As a result, the revised scheme produces an improved profile through significant enhancement of the reference-level drag ($Ek'G'/kG = 3.02$) and the vertical drag divergence at low levels. These results demonstrate that E and m' selectively control the magnitude of the drag for the subdomain including the downstream regions, while G' tends to almost equally enhance the drag regardless of the subdomains for this case.

From these and other experiments, we found that both the original and revised parameterization schemes tend to perform reasonably well for subdomain U (represented by negative OA) where an active wave-breaking region is not included. On the other hand, they perform relatively poorly for subdomain D (represented by positive OA) where an active wave-breaking region is included. The revised scheme, however, generally succeeds in producing low-level drag divergence. As far as the drag divergence or convergence is concerned, errors of the revised scheme are almost entirely confined in the convergence layers for case ME (see subdomain D in Fig. 19), indicating difficulties in treating such layers (see also section 4c).

For the series of mountain wave simulations performed in this study, we used $N = 0.01\ \mathrm{s}^{-1}$ and $U = 10\ \mathrm{m\ s}^{-1}$ to represent the lower troposphere. The Froude numbers for the three different mountain heights chosen in these simulations (i.e., 500 m, 1000 m, 1500 m) are 0.5, 1.0, and 1.5, which are below, at, and above the critical value (1.0) for wave breaking, respectively. To show how parameterization schemes perform for other flow conditions, we investigated an additional set of simulations for case ME (see Figs. 20b–e) representing different atmospheric structures given in Table 3. ($Fr \geqslant 1.0$ for these cases so that wave breaking occurs.) The simulated fields for cases ME2, ME3, ME4, and ME5 are qualitatively similar to one another and to that of case ME in that there is low-level wave breaking. (Some differences found in the downstream regions of cases ME4 and ME5 from other cases are caused by trapping of lee waves in low-level downstream regions propagating downstream due to nonhydrostaticity associated with smaller nondimensional halfwidth.[10]) The upper four panels of Fig. 21 show the parameterized results, which are qualitatively similar to those of case ME (shown in Fig. 19) despite the differences in the atmospheric structures. These results indicate that Fr is the leading factor in determining the characteristics of mountain waves, as far as mountains with a fixed shape are concerned. In addition, we considered a typical midlatitude winter condition (see Fig. 20f, case ME6) taken from McFarlane (1987, see his Fig. 2). Despite the presence of the vertical wind shear in the troposphere, wave breaking still occurs in the

---

[8] An increase of m results in an increase of τ. This increase of τ, however, results in a decrease of h_d and thus an increase of Ri_m. As a consequence, wave breaking is less likely to occur with larger m.

[9] $-1 \leqslant \mathrm{OA} \leqslant 1$; $0 \leqslant L_x \leqslant 1$; $C_m \Delta x = 1$ and $\delta = 1$.

[10] $b \equiv Na/U$.

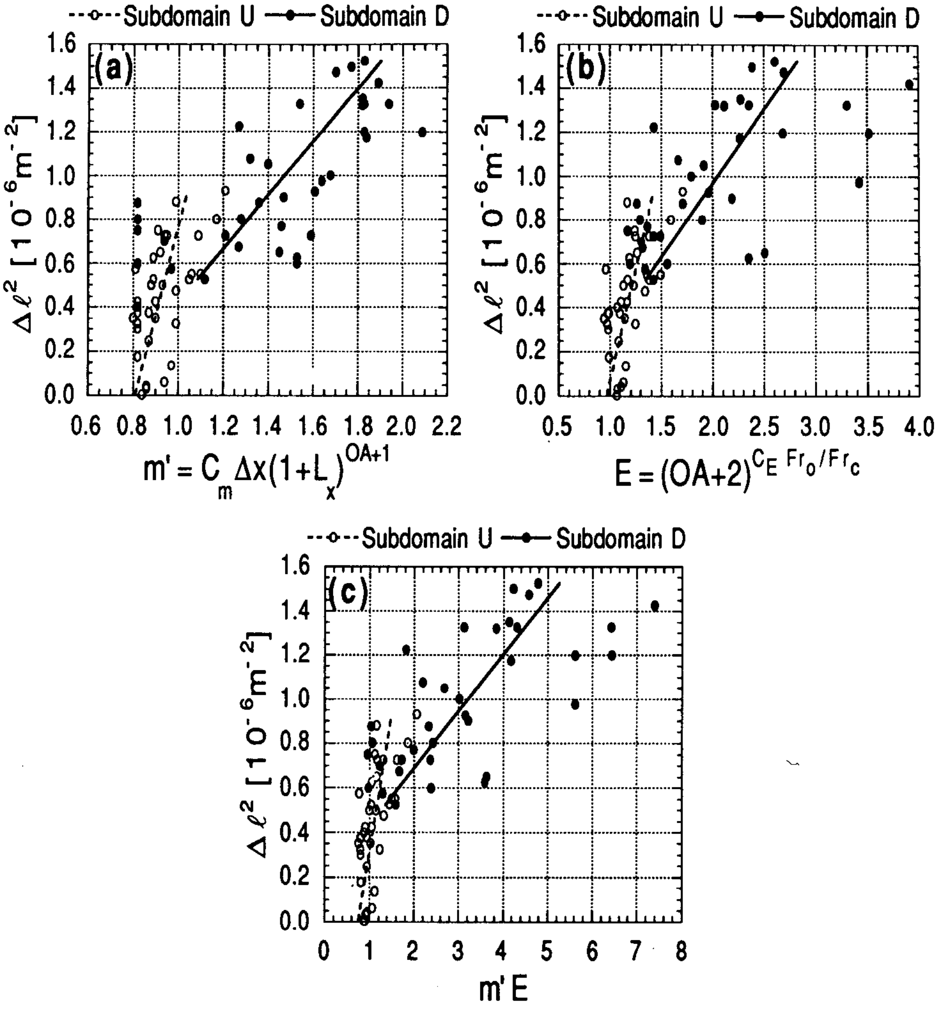

FIG. 18. As in Fig. 13 but for (a) m' and (b) E instead of Fr_0. Also shown is (c) for $m'E$.

downstream region although the depth of the wave breaking region is relatively shallow. The result with the schemes (Fig. 21e) shows the performance of the schemes at low levels similar to other cases.

5) ASSESSMENT OF THE REVISED SCHEME FOR DOMAINS CONTAINING BARRIERS WITH VARIOUS SHAPES

Although *Fr* more or less determines the characteristics of mountain waves for mountains with a fixed shape, the effect of mountain shape remains to be examined. We thus consider barriers of various shapes. First, as shown in Fig. 22, we choose extreme situations of case SA as a block barrier (or high plateau), case MI as a flat barrier (or low plateau), and case LK as a barrier with a peak to a plateau—which was considered a difficult case by Stern and Pierrehumbert (1988). Figure 22 displays parameterized drag profiles for these cases. Case SA (Fig. 22a) reveals almost complete upstream flow blocking and strong downstream wave breaking at low levels ($Fr = 1.5$). Although case SA has a barrier with deep vertical slopes, the revised scheme produces the divergence at low levels (Fig. 23a), whereas the original scheme fails to do so. Case MI (Fig. 22b) shows basically linear waves ($Fr = 0.5$) without wave breaking, and both schemes correctly produce no drag divergence or weak divergence due to dissipation of waves (Fig. 23b). The small peak in case LK (Fig. 22c) changes the flow to a weakly nonlinear flow ($Fr = 1.0$), and the revised scheme successfully produces the drag divergence at low levels (Fig. 23c).

Second, we choose cases LM and LN (Figs. 24a,b), which share the same values of SD and OC but have OA with opposite sign for subdomain *W*.[11] Case LM

---

[11] SD = 500 m, OC = 2.2, and OA = ∓ 0.11 for cases LM and LN, respectively.

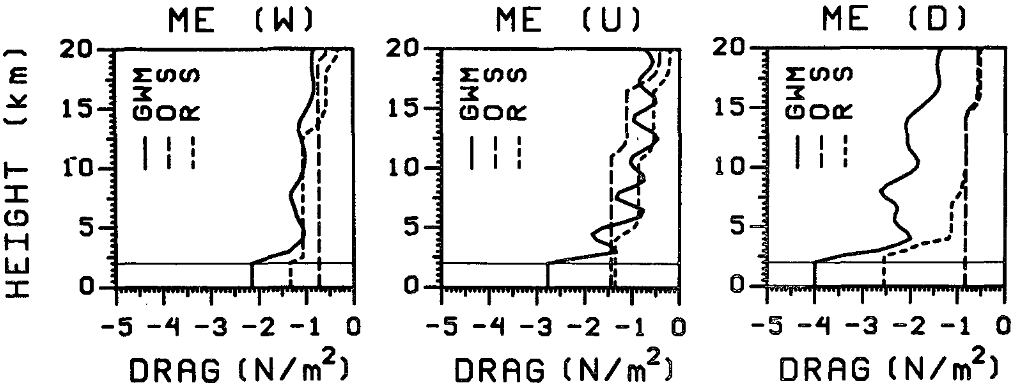

SD = 500.4 [m]	SD = 565.7 [m]	SD = 565.7 [m]
OA = 0	OA = -0.84	OA = 0.84
OC = 2.74	OC = 1.60	OC = 1.60
Fr_0 = 0.73	Fr_0 = 0.77	Fr_0 = 0.80
L_x = 0.24	L_x = 0.44	L_x = 0.44
E = 1.50	E = 1.10	E = 1.96
m = 3.60	m = 1.80	m = 1.80
m' = 2.05	m' = 0.87	m' = 1.61
k = 7.2×10^{-5} [m^{-1}]	k = 7.2×10^{-5} [m^{-1}]	k = 7.2×10^{-5} [m^{-1}]
Ek' = 6.2×10^{-5} [m^{-1}]	Ek' = 3.8×10^{-5} [m^{-1}]	Ek' = 1.3×10^{-4} [m^{-1}]
G = 0.35	G = 0.37	G = 0.39
G' = 0.75	G' = 0.66	G' = 0.67
Ek'G'/(kG) = 1.82	Ek'G'/(kG) = 0.94	Ek'G'/(kG) = 3.02

FIG. 19. Comparison of the drag profiles obtained from the gravity wave model (solid line) with those from the original parameterization scheme (long dashed line) and the revised parameterization scheme (short dashed line) for the three subdomains of case ME shown in Fig. 7. The orographic statistics and related parameters are explained in the text.

includes stronger wave breaking and vertically propagating waves mainly in the downstream region, while case LN includes vertically propagating waves almost directly above the barrier. When zonally averaged, case LN appeared to be more strongly nonlinear in view of the zonally averaged drag profile obtained from the gravity wave model (not shown). This case was considered more strongly nonlinear also by the revised scheme, mainly through (positively) large OA. The revised scheme generally responded more sensitively to the regions of drag divergence than the original scheme [the results are given in Kim (1992)].

Third, we compare cases ME, MM, and ML (see Figs. 7 and 24c,d) as cases with different shapes of barriers in terms of the number of ridges (1, 2, and 4, respectively). These cases generate different waves. In terms of the orographic statistics, however, the three cases are indistinguishable[12] for subdomain *W*. The only parameter that distinguishes between the three cases is *Fr*, but it differs significantly[13] only between cases ME or MM and ML. It appears that better statistical measures or even higher moments of orographic statistics are needed to distinguish among these cases. A question then arises regarding the effect of valleys in cases MM and ML.

Emeis (1990) and Grisogono et al. (1993) considered that gravity waves generated by two two-dimensional bell-shaped ridges may interfere constructively or destructively with each other. Tampieri and Hunt (1985) noted that, depending upon the distance between the ridges and *Fr*, the flow in the valley between two ridges may become stagnant and thus separated from the flow above the valley, or the flow in the valley may be ventilated. It is thus possible that a series of closely spaced barriers behave like a single wide barrier. One such example is case ML shown in Fig. 24d

---

[12] SD = 500.4 m, OA = 0, OC = 2.74.

[13] $Fr_0^{ME} = 0.73$, $Fr_0^{MM} = 0.74$, $Fr_0^{ML} = 1.04$.

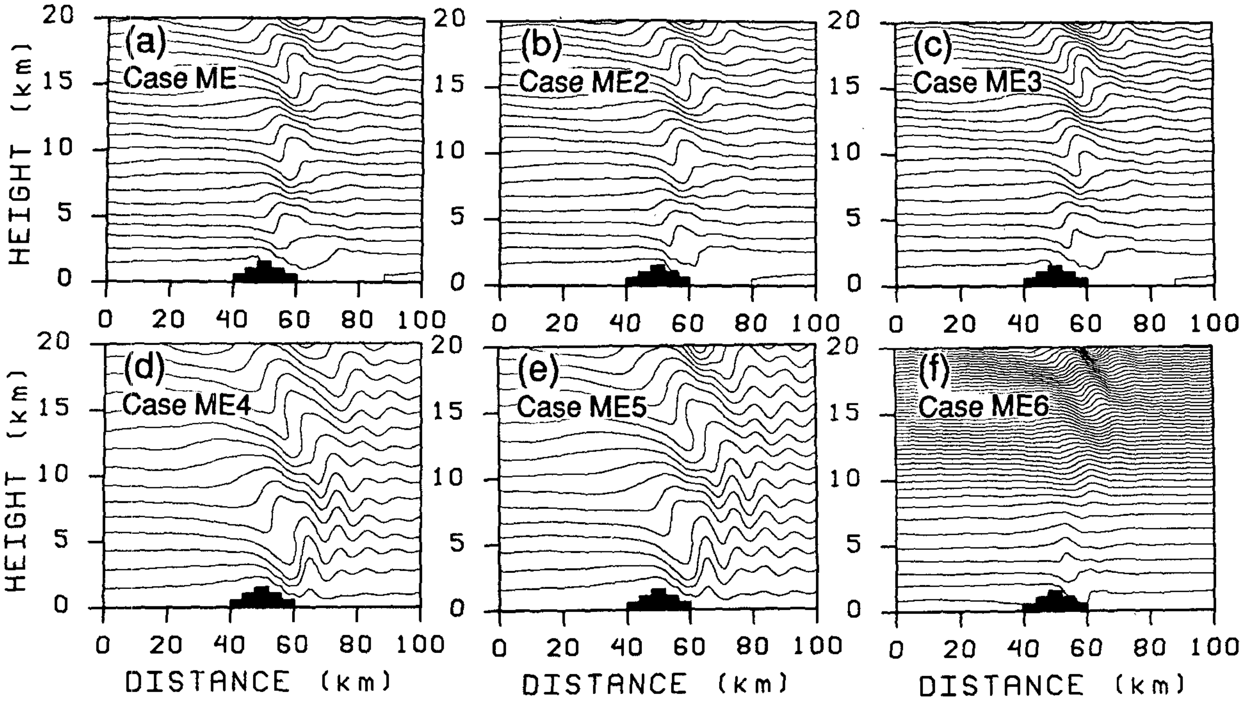

Fig. 20. Simulated potential temperature for barrier case ME with environmental conditions (a)–(e) of the values given in Table 3 and (f) of a typical midlatitude winter condition taken from McFarlane (1987). Contour intervals are different among the cases.

(vs case MB, Fig. 24f). Except for the small difference of the flow immediately above the barrier due to the weak penetration of the flow into the valley in case ML, the overall wave patterns are similar. As a counterexample, we also compare case MM (Fig. 24c) with case MC (Fig. 24e). These two cases seem to generate qualitatively similar waves at low levels, but case MM generates stronger waves due to the relatively strong penetration of the flow into the valley.

To see how these results affect the performance of the parameterization schemes, we compared the parameterized results for cases ME, MM, and ML (Kim 1992). The results show that the revised scheme generally produces stronger wave breaking for subdomain *D* at low levels than the original scheme. Moreover, we compared case MM with case MC, and case ML with case MB in terms of the orographic statistics and found that the difference in OC may serve as an additional measure[14] for distinguishing among barriers incorporating the "valley effect"; that is, the presence of valleys in a mountainous region increases the drag. This problem may be associated with the "envelope orography" that enhances large-scale orography by "filling up" the valleys. To determine how effectively valleys in mountainous regions affect the performance of parameterization schemes, however, more extensive investigation will have to be performed with a three-dimensional model.

6) Statistical assessment of the revised scheme

Finally, we collect statistics from a series of experiments performed with the dataset. Figures 25a,b show the correlation between τ_0 obtained from the gravity wave model and from the original parameterization scheme and the correlation between τ_0 obtained from the gravity wave model and from the revised parameterization scheme, respectively.[15]

We also examined the drag divergences at low levels (not shown). We found that the correlation between the model-simulated drag divergence and the parameterized divergence obtained from the revised scheme (0.4) is higher than the corresponding correlation with

---

[14] Larger OC corresponds to larger G' resulting in larger τ_0. We use OC to parameterize this relationship between G and τ_0 by assuming a simple linear relationship between G and OC.

[15] We designed the revised scheme in such a way that the drag and its divergence are allowed to be underestimated for some cases but not overestimated. Figure 25 shows that the revised scheme systematically underestimates the reference-level drag. One may suggest to systematically increase the magnitude of the reference-level drag, but this tends to produce excessively large drag divergence at high levels when the scheme fails to produce adequate drag divergence at low levels (e.g., Figs. 10c,i).

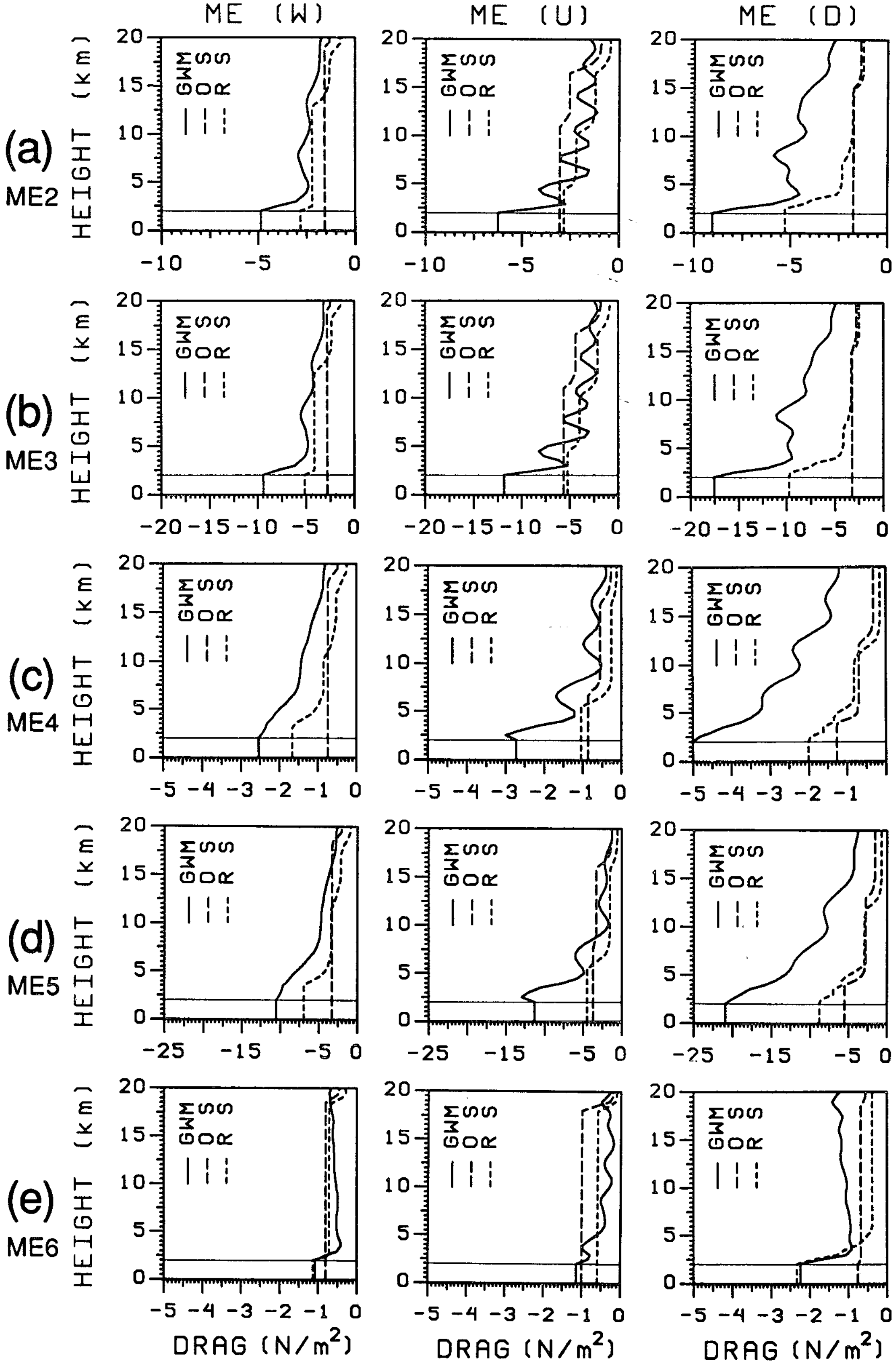

FIG. 21. As in Fig. 19 but for cases (a) ME2, (b) ME3, (c) ME4, (d) ME5, and (e) ME6 shown in Figs. 20b–f, respectively.

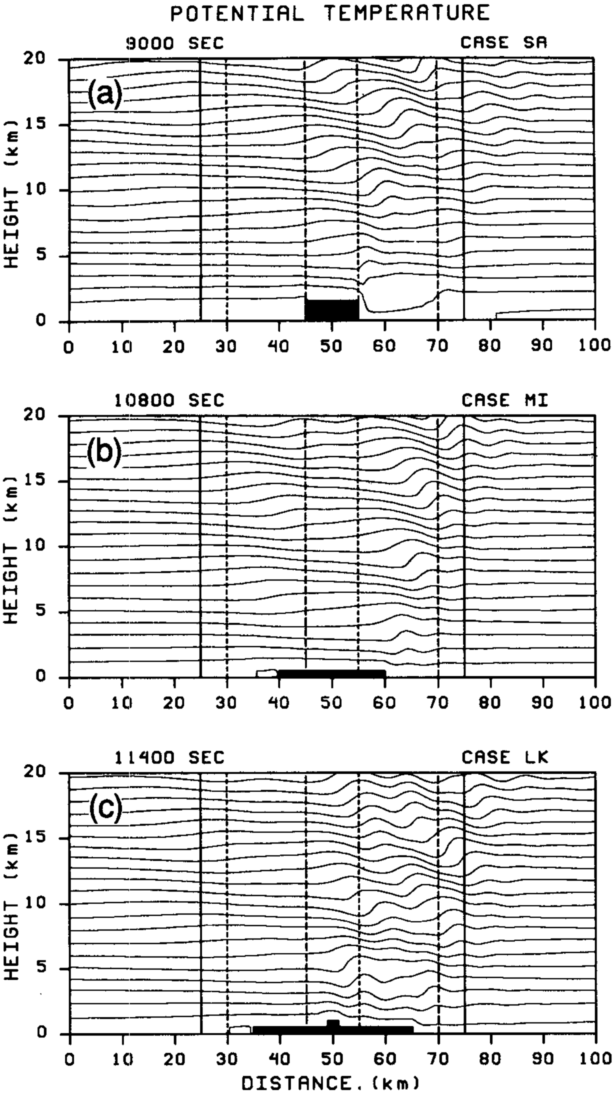

FIG. 22. As in Fig. 7 but for cases (a) SA, (b) M, and (c) LK.

the original scheme (0.2). Furthermore, we calculated the root-mean-square (rms) error of the acceleration due to the drag divergences from the statistics. We found the rms difference between the model-simulated acceleration and that from the original scheme, and the corresponding rms difference using the revised scheme are 530 and 373 m s^{-1} day^{-1}, respectively. These statistics show that the performance of the revised scheme is, in a statistical sense, superior to that of the original scheme.

7) SUMMARY OF THE CHARACTERISTICS OF THE REVISED SCHEME

Based on our experiments and analyses, we summarize the characteristics of the revised scheme as follows:

- The magnitude of the reference-level drag is determined by the statistics of sub-grid-scale orography in a grid interval and by the characteristics of the flow.
- Together with the Froude number, the additional statistical measures of orography, that is, Orographic Asymmetry and Convexity, are used to represent the effect of low-level wave breaking and the valley effect, respectively.

In conclusion, our results suggest that the effect of low-level wave breaking, that is, enhancement of low-level drag, is more adequately represented in the revised scheme through the selective enhancement of the reference-level drag with the aid of the additional statistical measures of orography.

c. Some considerations on the implementation of gravity wave parameterization schemes into large-scale models

Most of the existing parameterization schemes are based mainly on two-dimensional linear stationary hydrostatic mountain wave theory. In this section, we discuss problems that arise from such simplifications (including those unique to our revised scheme) for more general situations in large-scale models.

1) MAINTENANCE OF AN INVARIANCE PROPERTY OF PARAMETERIZED DRAG WITH RESPECT TO THE CHOICE OF GRID

In this paper, we evaluated parameterization schemes for a single domain that corresponds to a grid interval of large-scale models, while neglecting the upstream and/or downstream influence from nearby grid intervals. Due to the introduction of OA in the revised scheme, the parameterized drag depends on the location of the grid relative to orography. Since the revised scheme enhances the reference-level drag mainly through OA, the total drag is different for subdomains U and D of case ME (Fig. 7). In the continuous system, on the other hand, the total drag should be invariant. Thus, the selective enhancement of the drag by the revised scheme is done at the cost of violating the invariance property.

We may improve this situation, however, by considering a range of OA for sub-grid-scale orography in each grid interval. Assuming that the probability distribution of OA is uniform in that range, we calculate the expected value of the parameterized drag for each grid. This method includes both the upstream and downstream situations as extreme cases and thus is expected to reduce any systematic errors due to the violation of the invariance. Comparison of the results obtained from the two versions of the revised scheme showed qualitatively similar results for subdomain W, although the invariant version produced somewhat poorer results for subdomains D and U as anticipated (Kim 1992).

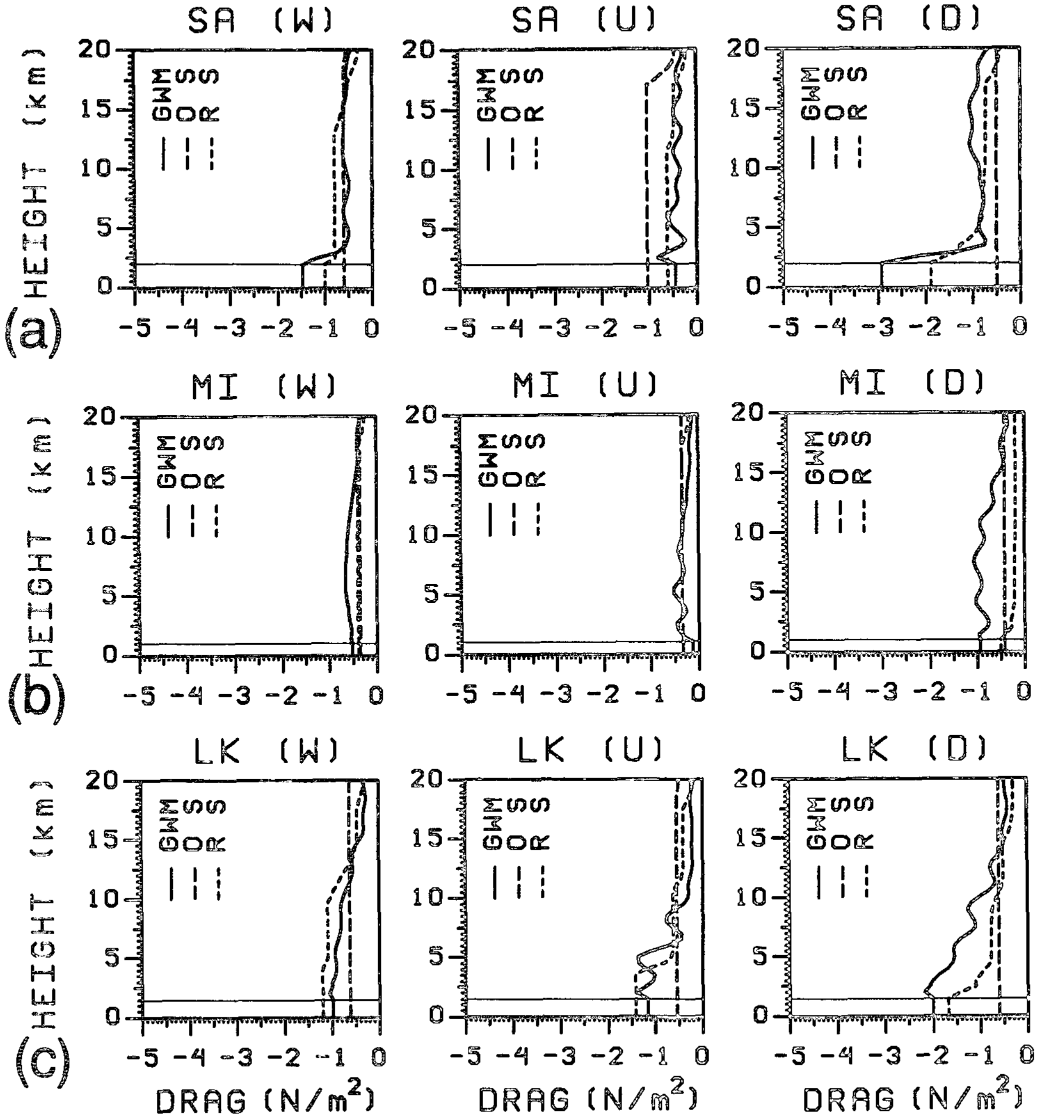

FIG. 23. As in Fig. 19 but for cases (a) SA, (b) MI, and (c) LK shown in Fig. 22.

2) PROPAGATION OF NONHYDROSTATIC WAVES TO NONOROGRAPHIC GRID INTERVALS

Another problem, which is related to the one above, is that parameterization schemes have been applied only to grid intervals containing sub-grid-scale orography (i.e., with nonzero SD). The flow in grid intervals with zero SD but just downstream of substantial sub-grid-scale orography may, however, experience considerable wave dissipation of nonhydrostatic waves propagated from the upstream grid interval. If it is necessary to include this effect in the parameterization, one possible way of coping with this situation is to extend the grid interval to include upstream mountains.

3) EFFECT OF MULTIPLE BARRIERS

Some barriers we considered in this study are clusters of closely arranged barriers for which the valley effect may be important, as discussed in section 4b. In real situations, however, we may have multiple barriers separated far from one another in one grid interval. In this case, we need to also consider the upstream and downstream influences of each barrier on other barriers. The question we first raise is whether our orographic statistics can properly handle this configuration of barriers. The general statistical parameters SD and OC can be applied to any irregular barriers. However, OA is designed originally for a single barrier. We thus performed a simple qualitative analysis of the upslope

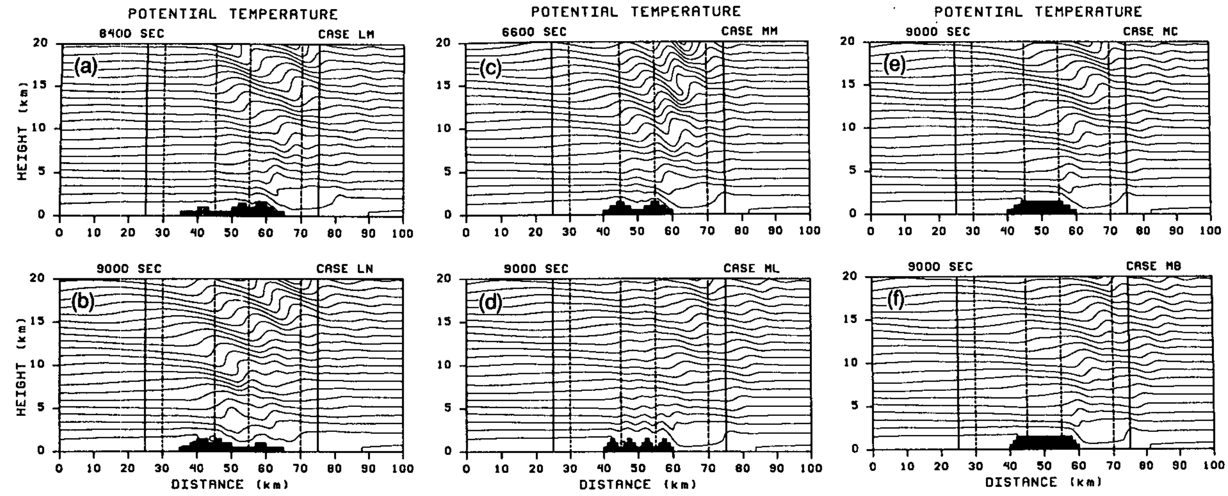

FIG. 24. As in Fig. 7 but for cases (a) LM, (b) LN, (c) MM, (d) ML, (e) MC, and (f) MB.

and downslope influences with configurations consisting of one or two barriers (described in Kim 1992). Our preliminary investigation suggests OA still roughly represents the combined upstream and downstream effects with double barriers. The inclusion of the effect of multiple barriers in the parameterization is, however, one of the remaining problems of the parameterization.

4) PARAMETERIZATION OF DRAG CONVERGENCE

In both observations and simulations of mountain waves, there are regions of vertical convergence (or decrease in magnitude) in vertical momentum or drag profiles—as well as regions of vertical divergence. The current status of orographic gravity wave drag parameterization, however, does not provide the means for treating regions of drag convergence. [This was also pointed out by Durran (1991).] One drawback due to this limit is that, even when the reference-level drag is accurately determined by the parameterization, the magnitude of the drag is often underestimated at upper levels. This is also one of the unsolved problems of the parameterization.

5) LIMITATION OF TWO-DIMENSIONAL MODELS

A very, in fact the most, important concern is the use of 2D models in studying parameterization of oro-

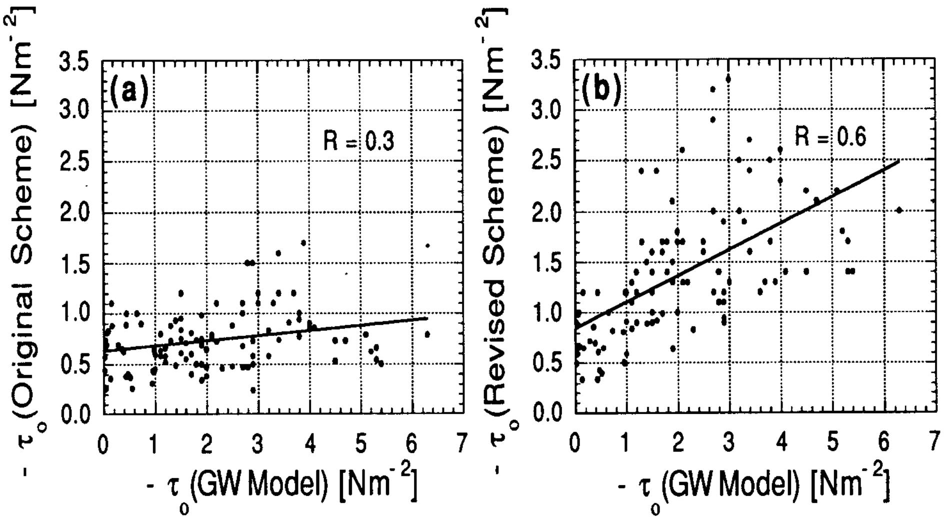

FIG. 25. Scatter plots of the reference-level drag (τ_0) simulated by the mesoscale gravity wave model vs (a) the reference-level drag parameterized by the original scheme and (b) that by the revised scheme. Statistics are obtained from 105 cases (3 subdomains × 35 simulations).

graphic gravity waves. Three-dimensional effects can drastically change the propagation characteristics of waves through increased dispersion. Smith (1989, see references therein) showed from 3D simulations that the horizontal mountain aspect ratio (r)—or the orientation of sub-grid-scale ridges—plays an important role in determining the onset of wave breaking, which might be happening excessively in the 2D simulations in which inherently large r is assumed.

The 3D effect has been taken into account for the parameterization of drag in the implementation stage by considering anisotropic orographic variance (e.g., Miller et al. 1989). Varying the critical Froude number for wave breaking as a function of r may be another way (see also a related study by Miranda and James 1992). We can also reduce the minimum Richardson number (4.6) by considering the enhancement of the vertical wind shear in a 3D wave system as discussed by Palmer et al. (1986). In our revised scheme, we calculate OA as an orientation-dependent measure partially incorporating the anisotropy of orography. The 3D effect of the waves is, however, not fully taken into account by these methods, and thus the inclusion of this effect in the parameterization remains as one of the challenging problems.

5. Summary

Parameterization of gravity waves due to sub-grid-scale orography is one of the crucial elements of most large-scale models of the atmosphere. Orographic gravity wave parameterization schemes for large-scale models of the atmosphere have been evaluated to date mainly on merits of overall improvement of simulated large-scale fields. Since this practice fails to take into account possible cancellation of errors from a variety of other sources, we used a mesoscale gravity wave model for evaluating parameterization schemes. In section 2, we introduced a numerical two-dimensional nonlinear anelastic nonhydrostatic mesoscale model, which we developed for simulating gravity waves over orography represented by rectangular blocks designed to simulate irregularities of real mountains. In section 3, we presented numerical simulations of mountain waves. We compared our model simulations with the corresponding analytic solutions of stratified flow over orography. We then performed simulations over various orography. We discussed some characteristics of simulated results in view of some important aspects of mountain waves such as wave breaking, resonant amplification of waves, and flow blocking.

In section 4, we constructed a test parameterization scheme by adopting some essential features of the existing schemes. We extensively evaluated the scheme using the dataset obtained from mountain wave simulations. Through a series of experiments, we found that the test scheme tends to poorly reproduce the effect of low-level wave breaking accompanied by resonant amplification of nonhydrostatic waves. The standard deviation of orographic height, which is the main statistical information regarding sub-grid-scale orography in the scheme together with the tuning coefficient, seems insufficient to properly parameterize this effect. We showed results suggesting that the vertical decrease of the Scorer parameter near the reference level is closely related to the vertical divergence of drag at low levels when wave breaking occurs, which can thus be used in the parameterization.

Also in section 4, in order to overcome the weakness of the test scheme we introduced the additional statistical measures of orography—the orographic asymmetry and convexity—as additional information on sub-grid-scale orography. Using the additional measures, we devised new parameters that are better related to the vertical variation of the Scorer parameter, which we regard as a measure of the nonlinear drag enhancement at low levels, than the Froude number. We revised the test scheme using the new parameters and extensively evaluated the revised scheme using the same dataset used for evaluating the test scheme. We obtained significantly improved results demonstrating the usefulness of the additional statistical measures of orography for improving the parameterization by better representing the effect of low-level wave breaking. We briefly investigated complexities caused by the valley effect and argued that the additional measures may also be useful for taking the valley effect into account in the parameterization. We also discussed some concerns in implementing parameterization schemes in large-scale models.

6. Discussion

Observations show that gravity waves break not only in the lower stratosphere but also in the lower troposphere. Wave breaking at low levels is the rule rather than exception over relatively broad and high mountains for typical atmospheric conditions (Pierrehumbert 1986). The nature of low-level wave breaking is highly transient, but its magnitude is significant. Observations show that the surface drag can be significantly enhanced due to low-level wave breaking (e.g., Smith 1978). Based on numerical simulations of nonlinear mountain waves, Peltier and Clark (1986) noted that excessive momentum flux over the amount required for the saturation is not necessarily deposited into the mean flow at breaking levels but may be directed downward, thereby increasing drag at low levels. Bacmeister and Schoeberl (1989) also showed through numerical simulations that a large divergence of momentum flux occurs not only at wave breaking levels but also below the lowest overturning region.

The effect of nonlinear drag enhancement due to low-level wave breaking and its potential importance for the parameterization of orographic gravity waves have been discussed by many authors (e.g., Chouinard et al. 1986; Palmer et al. 1986; Pierrehumbert 1986; Peltier and Clark 1986; McFarlane et al. 1987; Miller et al. 1989; Bacmeister 1993) but usually not explicitly incorporated into parameterization schemes. A notable exception is Miller et al. (1989), who relaxed the cutoff limit for SD (see Table 2) to generate "substantial low-level wave breaking" (see their Fig. 15b). Besides, although not implemented in a large-scale model, Pierrehumbert (1986) designed an alternate flux function for strongly nonlinear flow in an attempt to parameterize this effect of low-level wave breaking, that is, to enhance drag divergence at low levels. [See Pierrehumbert's (1986) expression for τ_0 in the bracket in Table 1 or his equation (3.10).] Moreover, simple drag profiles, which monotonically decrease with height, have been tested and/or implemented in some models (e.g., Pierrehumbert 1986; Stern et al. 1987; Stern and Pierrehumbert 1988; Laursen and Eliasen 1989; Broccoli and Manabe 1992). The parameterization may then be improved through intensifying drag divergence at low levels (as well as at upper levels), compared with the parameterization based on the saturation hypothesis, if the reference level is placed at a sufficiently low level where low-level wave breaking occurs.

We argue, however, based on our mesoscale simulations that these methods may not systematically distinguish between wave breaking and nonbreaking situations at low levels, the former of which can significantly enhance the magnitude of drag. In this study, we have shown results suggesting that the nonlinear drag enhancement due to low-level wave breaking is not properly included if the parameterization is based mainly on *Fr* only (see Fig. 13). In contrast to *Fr*, the new measures m' and E (Fig. 18) statistically better represent the drag enhancement. Consequently, the reference-level drag (see Fig. 25) and its vertical distribution (see section 4b) are, in general, better parameterized by the revised scheme.

Most existing schemes do not seem to systematically distinguish between two physical mechanisms for low-level drag with opposite impact; the decrease of drag due to upstream flow blocking and the enhancement of drag due to downstream wave breaking. It seems that a balance between these two opposite effects determines the magnitude of the reference-level drag. The revised scheme presented in this paper provides a way of resolving this problem by distinguishing these two, considering the upstream and downstream effects on the drag; that is, decreasing the drag in the upstream region and enhancing the drag in the downstream region. This study is, however, conducted with the framework of two-dimensional numerical simulations, and thus an adjustment of parameters may be necessary in its application to a 3D large-scale model.

There still remain many uncertainties and deficiencies concerning the basic assumptions in parameterizing gravity waves. In this study, we have shown our efforts to include the effect of low-level wave breaking. [See Kim and Arakawa (1994) for a preliminary result from a diagnostic application of the revised scheme to global monthly mean data.] Other examples of physical processes not incorporated in the parameterization, to our knowledge, are wave transience (e.g., Dunkerton 1981; Clark and Farley 1984; Peltier and Scinocca 1990 and references therein; Laprise 1993; Lott and Teitelbaum 1993), surface friction (e.g., Richard et al. 1989), radiation and clouds (e.g., Weissbluth and Cotton 1989; Durran and Klemp 1982b, 1983), effect of multiple waves or superposition of waves (e.g., Fritts 1985; Schoeberl 1985), and nonlinearity (e.g., Weissbluth and Cotton 1989; Smith 1993 and the references therein). It may be necessary to include these processes in future parameterizations of gravity wave drag.

Acknowledgments. We thank Professors Carlos Mechoso, Morton Wurtele, Steven Krueger, and Dr. Dan Landau for valuable comments. We also thank Dr. Paul E. Long and anonymous reviewers for careful review and constructive comments. Support was provided jointly by NSF under Grants ATM-8910564 and ATM-9224863, NASA under Grants NAG 5-789 and NAG 5-2224, and the DOE under Grant DE-FG03-91ER61214. Computing resources were obtained from the NCAR Scientific Computing Division, the Office of Academic Computing, and the Department of Atmospheric Sciences at UCLA.

APPENDIX A

Determination of the Master Turbulence Length Scale

For mountain wave simulations, the first-order turbulence closure scheme by Lilly (1962) is often used:

$$K_M = (k\Delta)^2 |Def| (1 - Ri)^{1/2}, \quad Ri \leqslant 1, \qquad (A.1)$$

where $\Delta \equiv (\Delta x \Delta z)^{1/2}$ and $k = 0.21$.

If the last two terms in (2.10) balance with each other, on the other hand, we obtain the relation

$$q = (\Lambda_1 l_1)^{1/2} |Def| \left(1 - \frac{l_2}{l_1} Ri\right)^{1/2}, \qquad (A.2)$$

where $(l_1, l_2, \Lambda_1) \equiv (A_1, A_2, B_1) l_m = (0.92, 0.74, 16.6) \times l_m$ (from Mellor and Yamada 1982).

To determine l_m, we use the formal analogy between (A.1) and (A.2) with $K_M \sim q l_1$. We then let $(k\Delta)^2 \sim (\Lambda_1 l_1)^{1/2} l_1$ for $Ri \approx 0$, yielding the following expression:

$$l_m = k(\Delta x \Delta z)^{1/2} A_1^{-3/4} B_1^{-1/4}. \qquad (A.3)$$

With the values given above, we obtain $l_m \sim 0.11 \times (\Delta x \Delta z)^{1/2}$. For the resolutions used for most of the simulations performed in this study; that is, $\Delta x = 1000$ m and $\Delta z = 500$ m, we find $l_m \sim 78$ m.

TABLE B1. Orographic statistics for case ME with Δz = 500 m, shown in Fig. 15.

Subdomain range	*W* 25 ~ 75 km	*U* 30 ~ 55 km	*D* 45 ~ 70 km
$\bar{x}$ [km]	51.5	44.0	59.0
Mode [km]	51.5	50.1	52.9
σ_x [km]	14.4	7.2	7.2
$\bar{h}$ [km]	360.0	600.0	600.0
σ_h (SD) [km]	500.4	565.7	565.7
N_x	50	25	25
N_B	20	15	15
N_T	36	30	30
OA	0.00	−0.84	0.84
OC	2.74	1.60	1.60

APPENDIX B

Additional Statistical Measures of Orography

We define the Orographic Asymmetry and Convexity for a grid interval Δx of a large-scale model (Kim and Arakawa 1991) as

Orographic Asymmetry (OA)

$$\equiv \frac{\bar{x} - \text{Mode}}{\sigma_x};$$

$$\text{Mode} \equiv \frac{\sum_{j=1}^{N_B} x_j n_j}{N_T};$$

$$\text{Orographic Convexity (OC)} \equiv \frac{\sum_{j=1}^{N_x} (h_j - \bar{h})^4}{N_x \sigma_h^4}, \quad \text{(B.1)}$$

where the overbars represent the horizontal average over the grid interval; N_T, N_B, and N_x denote the total number of blocks in the barrier, the number of bottom blocks in the barrier, and the number of grid intervals for the large-scale domain being considered, respectively; n_j is the number of blocks in the jth column of the large-scale domain so that $\sum_{j=1}^{N_x} n_j = N_T$; and σ_x and σ_h (=SD) are the standard deviations of the horizontal distance and the orographic height, respectively, defined by

$$\sigma_x \equiv \left(\frac{\sum_{j=1}^{N_x} (x_j - \bar{x})^2}{N_x} \right)^{1/2},$$

$$\sigma_h \equiv \left(\frac{\sum_{j=1}^{N_x} (h_j - \bar{h})^2}{N_x} \right)^{1/2}. \quad \text{(B.2)}$$

The values of these definitions and orographic statistics for case ME (Fig. 15) are tabulated in Table B1. For more cases see Kim (1992).

REFERENCES

Alpert, J. C., M. Kanamitsu, P. M. Caplan, J. G. Sela, G. H. White, and E. Kalnay, 1988: Mountain induced gravity wave drag parameterization in the NMC medium-range forecast model. Preprints, *Eighth Conf. on Numerical Weather Prediction,* Baltimore, MD, Amer. Meteor. Soc., 726–733.

Arakawa, A., 1966: Computational design for long-term numerical integration of equations of fluid motion: Two dimensional incompressible flow. Part I. *J. Comput. Phys.,* **1,** 119–143.

Bacmeister, J. T., 1993: Mountain-wave drag in the stratosphere and mesosphere inferred from observed winds and a simple mountain-wave parameterization scheme. *J. Atmos. Sci.,* **50,** 377–399.

——, and M. R. Schoeberl, 1989: Breakdown of vertically propagating two-dimensional gravity waves forced by orography. *J. Atmos. Sci.,* **46,** 2109–2134.

Bannon, P. R., and J. A. Yuhas, 1990: On mountain wave drag over complex terrain. *Meteor. Atmos. Phys.,* **43,** 155–162.

Boer, G. J., N. A. McFarlane, R. Laprise, J. D. Henderson, and J.-P. Blanchet, 1984: The Canadian Climate Centre spectral atmospheric general circulation model. *Atmos.–Ocean,* **22,** 397–429.

Broccoli, A. J., and S. Manabe, 1992: The effects of orography on midlatitude Northern Hemisphere dry climates. *J. Climate,* **5,** 1181–1201.

Chouinard, C., M. Beland, and N. McFarlane, 1986: A simple gravity-wave drag parameterization for use in medium-range weather forecast models. *Atmos. Ocean,* **24,** 91–110.

Clark, T. L., and R. D. Farley, 1984: Severe downslope windstorm calculates in two and three spatial dimensions using anelastic interactive grid nesting: A possible mechanism for gustiness. *J. Atmos. Sci.,* **41,** 329–350.

——, and W. R. Peltier, 1984: Critical level reflection and the resonant growth of nonlinear mountain waves. *J. Atmos. Sci.,* **41,** 3122–3134.

Dunkerton, T. J., 1981: Wave transience in a compressible atmosphere. Part I: Transient internal wave, mean-flow interaction. *J. Atmos. Sci.,* **38,** 281–297.

Durran, D. R., 1986: Another look at downslope windstorms. Part I: The development of analogs to supercritical flow in an infinitely deep, continuously stratified fluid. *J. Atmos. Sci.,* **43,** 2527–2543.

——, 1990: Mountain waves and downslope winds. *Atmospheric Processes over Complex Terrain, Meteor. Monogr.,* No. 23, W. Blumen, Ed., Amer. Meteor. Soc., 59–81.

——, 1991: Orographic wave drag on the lower troposphere: The importance of trapped waves. Preprints, *Eighth Conf. on Atmospheric and Oceanic Waves and Stability,* Denver, CO, Amer. Meteor. Soc., 377–380.

——, and J. B. Klemp, 1982a: On the effects of moisture on the Brunt–Väisälä frequency. *J. Atmos. Sci.,* **39,** 2152–2158.

——, and ——, 1982b: The effects of moisture on trapped mountain lee waves. *J. Atmos. Sci.,* **39,** 2490–2506.

——, and ——, 1983: A compressible model for the simulation of moist mountain waves. *Mon. Wea. Rev.,* **111,** 2341–2361.

——, and ——, 1987: Another look at downslope winds. Part II: Nonlinear amplification beneath wave-overturning layers. *J. Atmos. Sci.,* **44,** 3402–3412.

Eliassen, A., and E. Palm, 1960: On the transfer of energy in the stationary mountain waves. *Geophys. Publ.,* **22,** 1–23.

Emeis, S., 1990: Surface pressure distribution and pressure drag on mountains. *Meteor. Atmos. Phys.,* **43,** 173–185.

Fritts, D. C., 1985: A numerical study of gravity wave saturation: Nonlinear and multiple wave effects. *J. Atmos. Sci.,* **42,** 2043–2058.

Gates, W. L., 1992: AMIP: The atmospheric model intercomparison project. *Bull. Amer. Meteor. Soc.,* **73,** 1962–1970.

Grisogono, B., S. C. Pryor, and R. E. Keislar, 1993: Mountain-wave drag over double bell-shaped orography. *Quart. J. Roy. Meteor. Soc.,* **119,** 199–206.

Helfand, H. M., J. C. Jusem, J. Pfaendtner, J. Tenenbaum, and E. Kalnay, 1987: The effects of a gravity-wave drag parameterization scheme on GLA fourth order GCM forecast. *J. Meteor. Soc. Japan,* (special volume for WMO/IUGG Numerical Weather Prediction Symp.), 729–742.

Huppert, H. E., and J. W. Miles, 1969: Lee waves in a stratified flow. Part 3. Semi-elliptical obstacle. *J. Fluid Mech.,* **35,** 481–496.

Iwasaki, T., S. Yamada, and K. Tada, 1989: A parameterization scheme of orographic gravity-wave drag with two different vertical partitionings. Part I: Impacts on medium-range forecasts. *J. Meteor. Soc. Japan,* **67,** 11–27.

Kim, J., and L. Mahrt, 1992: Momentum transport by gravity waves. *J. Atmos. Sci.,* **49,** 735–748.

Kim, Y.-J., 1992: Numerical simulation and parameterization of orographic gravity waves. Ph.D. dissertation, University of California, Los Angeles, 254 pp.

——, and A. Arakawa, 1991: Assessment of gravity wave parameterization schemes using a mesoscale gravity-wave model. Preprints, *Ninth Conf. on Numerical Weather Prediction,* Denver, CO, Amer. Meteor. Soc., 380–383.

——, and ——, 1994: Inclusion of the effect of low-level wave-breaking in orographic gravity-wave parameterization for large-scale models of the atmosphere. Preprints, *10th Conf. on Numerical Weather Prediction,* Portland, OR, Amer. Meteor. Soc., 386–388.

——, S. K. Kar, and A. Arakawa, 1993: A nonreflecting upper-boundary condition for anelastic nonhydrostatic mesoscale gravity-wave models. *Mon. Wea. Rev.,* **121,** 1249–1261.

Laprise, J. P. R., 1993: An assessment of the WKBJ approximation to the vertical structure of linear mountain waves: Implications for gravity-wave drag parameterization. *J. Atmos. Sci.,* **50,** 1469–1487.

Laursen, L., and E. Eliasen, 1989: On the effects of the damping mechanisms in an atmospheric general circulation model. *Tellus,* **41**A, 385–400.

Lilly, D. K., 1962: On the numerical simulation of buoyant convection. *Tellus,* **14,** 148–172.

——, 1972: Wave momentum flux—A GARP problem. *Bull. Amer. Meteor. Soc.,* **53,** 17–23.

——, and J. B. Klemp, 1979: The effects of terrain shape on nonlinear hydrostatic mountain waves. *J. Fluid Mech.,* **95,** 241–261.

Lindzen, R. S., 1981: Turbulence and stress owing to gravity wave and tidal breakdown. *J. Geophys. Res.,* **86,** 9707–9714.

——, 1988: Supersaturation of vertically propagating internal gravity waves. *J. Atmos. Sci.,* **45,** 705–711.

Lott, F., and H. Teitelbaum, 1993: Linear unsteady mountain waves. *Tellus,* **45**A, 201–220.

McFarlane, N. A., 1987: The effect of orographically excited gravity-wave drag on the general circulation of the lower stratosphere and troposphere. *J. Atmos. Sci.,* **44,** 1775–1800.

——, C. Girard, and D. W. Shantz, 1987: Reduction of systematic errors in NWP and general circulation models by parameterized gravity-wave drag. *J. Meteor. Soc. Japan,* (special volume for WMO/IUGG Numerical Weather Prediction Symp.), 713–728.

Mellor, G. L., and T. Yamada, 1982: Development of a turbulence closure model for geophysical fluid problems. *Rev. Geophys. Space Phys.,* **20,** 851–875.

Miller, M. J., and T. N. Palmer, 1986: Orographic gravity-wave drag: Its parameterization and influence in general circulation and numerical weather prediction models. *Proc. Seminar/Workshop on Observation, Theory and Modeling of Orographic Effects,* Vol. 1, Shinfield Park, Reading, United Kingdom, ECMWF, 283–333.

——, ——, and R. Swinbank, 1989: Parameterization and influence subgrid-scale orography in general circulation and numerical weather prediction models. *Meteor. Atmos. Phys.,* **40,** 84–109.

Miranda, P. M. A., and I. N. James, 1992: Non-linear three-dimensional effects on gravity-wave drag: Splitting flow and breaking waves. *Quart. J. Roy. Meteor. Soc.,* **118,** 1057–1081.

Palmer, T. N., G. J. Shutts, and R. Swinbank, 1986: Alleviation of a systematic westerly bias in circulation and numerical weather prediction models through an orographic gravity-wave drag parameterization. *Quart. J. Roy. Meteor. Soc.,* **112,** 1001–1039.

Peltier, W. R., and T. L. Clark, 1979: The evolution and stability of finite-amplitude mountain waves. Part II: Surface-wave drag and severe downslope windstorms. *J. Atmos. Sci.,* **36,** 1498–1529.

——, and ——, 1983: Nonlinear mountain waves in two and three spatial dimensions. *Quart. J. Roy. Meteor. Soc.,* **109,** 527–548.

——, and ——, 1986: Nonlinear mountain waves and wave-mean flow interaction: Elements of a drag parameterization. *Proc. Seminar/Workshop on Observation, Theory and Modeling of Orographic Effects.* Vol. 1, Shinfield Park, Reading, U.K., ECMWF, 223–249.

——, and J. F. Scinocca, 1990: The origin of severe downslope windstorm pulsations. *J. Atmos. Sci.,* **47,** 2853–2870.

Pierrehumbert, R. T., 1986: An essay on the parameterization of orographic gravity-wave drag. *Proc. Seminar/Workshop on Observation, Theory and Modeling of Orographic Effects,* Vol. 1, September, Shinfield Park, Reading, United Kingdom, ECMWF, 251–282.

Pihos, G. G., and M. G. Wurtele, 1981: An efficient code for the simulation of nonhydrostatic stratified flow over obstacles, NASA Contract Rep. CR-3385, 126 pp. [NTIS-N8123762.]

Richard, E., P. Mascart, and E. C. Mickerson, 1989: The role of surface friction in downslope windstorms. *J. Appl. Meteor.,* **28,** 241–251.

Roache, P. J., 1972: *Computational Fluid Dynamics.* Hermosa Publishers, 133–134.

Schoeberl, M. R., 1985: The penetration of mountain waves into the middle atmosphere. *J. Atmos. Sci.,* **42,** 2856–2864.

——, 1988: A model of stationary gravity wave breakdown with convective adjustment. *J. Atmos. Sci.,* **45,** 980–992.

Scorer, R. S., 1949: Theory of waves in the lee of mountains. *Quart. J. Roy. Meteor. Soc.,* **75,** 41–56.

Sharman, R. D., T. L. Keller, and M. G. Wurtele, 1988: Incompressible and anelastic flow simulations on numerically generated grid. *Mon. Wea. Rev.,* **116,** 1124–1136.

Smith, R. B., 1978: A measurement of mountain drag. *J. Atmos. Sci.,* **35,** 1644–1654.

——, 1985: On severe downslope winds. *J. Atmos. Sci.,* **42,** 2597–2603.

——, 1989: Hydrostatic airflow over mountains. *Advances in Geophysics,* Vol. 31, Academic Press, 1–41.

——, 1993: Stagnation points and bifurcation in 3-D mountain airflow. *Tellus,* **45**A, 28–43.

Stern, W. F., and R. T. Pierrehumbert, 1988: The impact of an orographic gravity-wave drag parameterization on extended range prediction with a GCM. Preprints, *Eighth Conf. on Numerical Weather Prediction,* Baltimore, MD, Amer. Meteor. Soc., 745–750.

——, ——, J. Sirutis, J. Ploshay, and K. Miyakoda, 1987: Recent development in the GFDL extended-range forecasting system. *J. Meteor. Soc. Japan,* (special volume WMO/IUGG NWP Symp.), 359–363.

Surgi, N., 1989: Systematic errors of the FSU global spectral model. *Mon. Wea. Rev.,* **117,** 1751–1766.

Takacs, L. L., 1985: A two-step scheme for the advection equation with minimized dissipation and dispersion errors. *Mon. Wea. Rev.,* **113,** 1050–1065.

Tampieri, F., and J. C. R. Hunt, 1985: Two-dimensional stratified fluid flow over valleys: Linear theory and a laboratory investigation. *Bound.-Layer Meteor.,* **32,** 257–279.

Walterscheid, R. L., and G. Schubert, 1990: Nonlinear evolution of an upward propagating gravity waves: Overturning, convection, transience and turbulence. *J. Atmos. Sci.,* **47,** 101–125.

Weissbluth, M. J., and W. R. Cotton, 1989: Radiative and nonlinear influences on orographic gravity wave drag. *Mon. Wea. Rev.,* **117,** 2518–2534.

Wilhelmson, R. B., and C.-S. Chen, 1982: A simulation of the development of successive cells along a cold outflow boundary. *J. Atmos. Sci.,* **39,** 1466–1483.

Wurtele, M. G., R. D. Sharman, and T. L. Keller, 1987: Analysis and simulations of a troposphere–stratosphere gravity wave model. Part I. *J. Atmos. Sci.,* **44,** 3269–3281.